Precambrian Research 305 (2018) 218–235

Contents lists available at ScienceDirect

Precambrian Research

journal homepage: www.elsevier.com/locate/precamres

Fe isotopes of a 2.4 Ga hematite-rich IF constrain marine redox conditions around the GOE

Margriet L. Lantink[a,*], Paul B.H. Oonk[a,b], Geerke H. Floor[c], Harilaos Tsikos[b], Paul R.D. Mason[a]

[a] Department of Earth Sciences, Utrecht University, P.O. Box 80.115, 3508 TC Utrecht, The Netherlands
[b] Geology Department, Rhodes University, Drosty Road, Grahamstown 6139, South Africa
[c] GFZ German Research Centre for Geosciences, Telegrafenberg, 14473 Potsdam, Germany

ARTICLE INFO

Keywords:
GOE
Iron isotopes
Hematite
Hotazel Formation

ABSTRACT

The hematite- and manganese-rich Hotazel iron formation, Griqualand West basin, South Africa, was deposited at a key moment in time, close to the GOE between 2.4 and 2.3 Ga. It stratigraphically overlies the Ongeluk Formation, comprising thick flood basalts, which in turn interfinger with and cover the Makganyene Formation diamictites, the inferred remnants of the first Paleoproterozoic Snowball Earth interval. No extensive research has been conducted to date on the basal part of the Hotazel Formation due to poor exposure, though it constitutes an important link between a period of large-scale ice cover, extensive volcanism and the onset of atmospheric oxygenation.

Here, we present a detailed petrographic, geochemical and Fe isotope study of a roughly 3-metre-long drill-core exposing the Ongeluk to Hotazel contact. Our results show that after the cessation of Ongeluk volcanism, primary precipitation of Fe(III) oxyhydroxides from the photic surface zone of the original basin became the dominant sedimentation mechanism. Negative δ^{56}Fe values (between −0.26 and −0.50‰) in micro-drilled hematite-rich chert indicate that surface water δ^{56}Fe compositions at the time of deposition were depleted. Yet, δ^{56}Fe and bulk-rock Fe/Mn values are still substantially higher (1–2‰) than those reported higher up in the Mn-rich layers of the Hotazel sequence, suggesting that redox potentials were still comparatively limited during the earliest stages of the Hotazel depositional environment.

The base of the Hotazel Formation thus forms a transitional interval between precipitation from essentially ferruginous seawater, as recorded in the Ghaap Group BIFs, and from isotopically and chemically highly evolved surface waters, as demonstrated by the Hotazel Mn-rich layers. In the absence of Fe(II) as a strong reducing agent, large volumes of photosynthetic oxygen may have eventually escaped into the atmosphere, leading to the onset of atmospheric oxygenation. Our results thus contradict previous models that place the onset of the GOE before the Hotazel Formation, concurrent with and mechanistically linked to the Makganyene and Ongeluk events. Instead, we show that the Hotazel basal sediments are still pre-GOE, consistent with their circa 2.4 Ga age and the continuation of MIF-S higher in the stratigraphic record.

1. Introduction

Unlike today, anoxic conditions prevailed in the deep oceans during most of Earth's history (Holland, 1984; Canfield, 1998). There is widespread evidence in the rock record for a permanent rise in atmospheric O_2 levels somewhere between 2.4 Ga and 2.1 Ga, termed the Great Oxidation Event (GOE) (Holland, 1984, 2006, 1999). Strong evidence is provided by the loss of mass-independent fractionation of sulphur isotopes (MIF-S) in the sedimentary record after 2.3 Ga, dating the time when pO_2 levels rose above 10^{-5} times the present atmospheric value (Farquhar et al., 2000; Pavlov and Kasting, 2002; Bekker et al., 2004). Nevertheless, the precise nature and evolution of ocean redox conditions around the GOE remains unknown.

The O_2 that was introduced into the atmosphere during the GOE ultimately originated from marine prokaryotes (e.g. Buick, 2008; Campbell and Allen, 2008). Paradoxically, widespread deposition of iron formation (IF), either banded (BIF) or granular (GIF), took place until approximately 1.8 Ga (Bekker et al., 2010), indicating that the oceans were ferruginous (anoxic and Fe^{2+}-rich) long after the GOE (e.g. Planavsky et al., 2011; Poulton and Canfield, 2011; Reinhard et al., 2013). Meanwhile, the presence of hematite (Fe_2O_3) in IF has been used to argue for an O_2-bearing water column (e.g. James, 1954; Morris,

* Corresponding author.
E-mail addresses: m.l.lantink@uu.nl (M.L. Lantink), geerke.floor@gfz-potsdam.de (G.H. Floor), H.Tsikos@ru.ac.za (H. Tsikos).

https://doi.org/10.1016/j.precamres.2017.12.025
Received 9 June 2017; Received in revised form 30 November 2017; Accepted 4 December 2017
Available online 06 December 2017
0301-9268/

1993; Beukes and Gutzmer, 2008; Hoashi et al., 2009; Smith et al., 2013). Recent indications for oxygenic photosynthesis much older than the onset of the GOE (Brasier et al., 2006; Eigenbrode and Freeman, 2006; Summons et al., 2006; Anbar et al., 2007; Buick, 2008; Eigenbrode et al., 2008; Waldbauer et al., 2009; Konhauser et al., 2017 and references therein) promoted the idea of a locally redox-stratified pre-GOE ocean. In shallow parts of the ocean, oxygenic photosynthesis allowed for the accumulation of O_2 in so-called *oxygen oases* (Olson et al., 2013; Riding et al., 2014) and caused progressive oxidation and precipitation of Fe. However, anaerobic photosynthetic bacteria are equally capable of oxidising Fe^{2+} (e.g. Widdel et al., 1993; Konhauser et al., 2002) and thus the presence of hematite in IF proves to be inconclusive for the availability of free O_2 (e.g. Kappler et al., 2005; Czaja et al., 2012; Li et al., 2013). Given this, late Archean and early Proterozoic IFs may predominantly reflect enhanced global magmatism rather than increasing O_2 levels.

Iron isotopes are a key redox proxy for the evolution of O_2 in the oceans (e.g. Beard et al., 1999, 2003; Anbar et al., 2000; Bullen et al., 2001; Sharma et al., 2001; Skulan et al., 2002; Welch et al., 2003; Johnson et al., 2002, 2005; Rouxel et al., 2003, 2005; Severmann et al., 2004) since redox reactions involving iron are accompanied by significant isotope fractionation. Recent Fe (and Mo) isotope studies on South African IFs have provided strong clues for the existence of an O_2-stratified pre-GOE water column (Czaja et al., 2013; Planavsky et al., 2014; Satkoski et al., 2015; Kurzweil et al., 2016). However, probably most of the O_2 produced was readily consumed by the large reducing potential of the Earth's ancient oceans which kept atmospheric O_2 levels generally low. A shift in balance between O_2 sources and sinks after 2.45 Ga allowed permanent accumulation of O_2 in the atmosphere (Lyons et al., 2014). Several models have sought for an explanation in changes in volcanic input (Claire et al., 2006; Zahnle et al., 2006; Kump and Barley, 2007; Gaillard et al., 2011). However, up to this point the role of the oceans at the exact timing of the GOE remains highly ambiguous.

A new, reliable U-Pb age of 2426 ± 3 Ma for the Ongeluk volcanics from the Transvaal basin, South Africa (Gumsley et al., 2017) places the stratigraphically overlying manganiferous IF deposits of the Hotazel Formation at an age of circa 2.4 Ga. The Hotazel strata therefore potentially yield key information on the ocean redox conditions either immediately prior to or during the GOE. Tsikos et al. (2010) reported very depleted bulk-rock $\delta^{56}Fe$ values down to −2.4‰ in all hematite- and Mn-rich layers of the Hotazel Formation. They interpreted these to represent a Rayleigh fractionation process, in which the protracted oxidation of Fe^{2+} (from a large reservoir with $\delta^{56}Fe$ = 0‰) and subsequent raining out of the heavy Fe isotopes eventually resulted in an isotopically depleted residual Fe(II) pool. These Fe isotopic characteristics, and furthermore the uniquely voluminous sedimentary Mn deposits (Laznicka, 1992), advocate the Hotazel Formation as potentially one of the terminal Paleoproterozoic marine sinks for photosynthetic O_2 that may actually have triggered the onset of the GOE.

Other paleodepositional models place the Hotazel Formation in a post-glacial, post-GOE (i.e. oxygenated) world (Kirschvink et al., 2000; Kopp et al., 2005; Kirschvink and Kopp, 2008; Gumsley et al., 2017). They interpret the Makganyene diamictite, which stratigraphically underlies and interfingers with the Ongeluk volcanics, to represent the end of the first global glaciation ("Snowball Earth") at the onset of significant atmospheric oxygenation. Extensive Mn(IV) deposition in an oxygenated marine environment would have taken place due to ice cap retreat in the aftermath of the Makganyene glacial event.

To test the validity of the proposed models, we focus here on a three metre thick interval that uniquely captures the bottom part of the Hotazel Formation and its contact with the Ongeluk volcanics underneath. We study this part of the stratigraphy in a pristine drill-core section for the first time and investigate a crucial link between large-scale ice cover retreat, extensive flood basalt formation, and the onset of the GOE.

Detailed petrographic, geochemical and Fe isotopic analysis has been carried out on these rocks to examine the paleodepositional setting during the earliest phase of Hotazel deposition, after cessation of the Ongeluk volcanism, and to identify the redox conditions of the original water column at that time. Since the Fe incorporated in the crystal lattice of primary hematite is thought to have reflected initial oxidation of Fe^{2+} in the water column (Ayres, 1972; Ahn and Buseck, 1990; Beukes and Gutzmer, 2008; Smith et al., 2013), Fe isotope analysis was carried out for the hematite-rich parts of the Hotazel Formation and bulk-rock analysis for the Ongeluk volcanics. Our results not only provide constraints on local paleoenvironmental conditions at the initial stages of the Hotazel deposition, but contribute in a wider context to our understanding of the redox evolution of the Transvaal basin and its relation to the GOE.

2. Geological setting

The Hotazel Formation constitutes the upper part of the late Archean to early Proterozoic Transvaal Supergroup, deposited in the partly enclosed Transvaal basin (e.g. Beukes, 1983), at the margins of the ancient supercontinent of Vaalbara (Button, 1976; Cheney, 1996; de Kock et al., 2009). The stratigraphy of the Transvaal Supergroup in the Griqualand West Basin is divided into two Groups (Fig. 1a). The lower ca 1.6 km thick Ghaap Group was deposited between 2.64 and 2.45 Ga (Pickard, 2003; Beukes and Gutzmer, 2008) and consists of a thick succession of mainly dolomitic carbonates at the base (Campbellrand subgroup), which are overlain by several hundreds of metres of BIF stratigraphy of the Asbestos Hills and Koegas Subgroups (Klein and Beukes, 1989; Beukes and Klein, 1990; Beukes and Gutzmer, 2008).

The stratigraphically higher Postmasburg Group begins with the glacial diamictites of the Makganyene Formation. These are covered by a thick (300–900 m) package of tholeiitic basaltic andesites from the subaqueously extruded Ongeluk Formation as indicated by pillow lavas, hyaloclastites and massive flows (Grobler and Botha, 1976; Schütte, 1992; Cornell and Schütte, 1995; Cornell et al., 1996). The Ongeluk volcanics are overlain by the chemical sediments of the ca 100–150-metre-thick Hotazel Formation (Fig. 1b), which is characterised by three distinct Mn-ore layers, inter-layered with magnetite-carbonate BIF. At the contact between the BIF and Mn-bands, transitional lutites occur (i.e. fine-grained cherty iron formation), ranging in thickness from a few decimeters up to several metres (Gutzmer and Beukes, 1996; Tsikos et al., 2003, 2010). These lutites are rich in hematite and Mn-carbonates. The Hotazel Formation is unconformably overlain by carbonates of the Mooidraai Formation, which represents a shallow-marine platform succession (Swart, 2012).

The depositional age of the Hotazel Formation and hence its relative timing with regard to the GOE has long been a topic of debate. The Ongeluk volcanics were initially dated by Cornell et al. (1996) at ca 2222 ± 13 Ma. By implication, depositional models placed the timing of the Hotazel after the GOE (Schütte, 1992; Cornell and Schütte, 1995; Cornell et al., 1996; Kirschvink et al., 2000; Kopp et al., 2005; Kirschvink and Kopp, 2008). One model explained the Fe-Mn sediments of the Hotazel to reflect pulses of strong hydrothermal fluid input (related to the Ongeluk volcanic activity) and rapid precipitation upon oxidation with the oxygenated seawater (Schütte, 1992; Cornell and Schütte, 1995; Cornell et al., 1996). More recent models related the deposition of Mn ore bodies to primary precipitation of Mn(IV) in a post-Snowball Earth environment (Kirschvink et al., 2000; Kopp et al., 2005; Kirschvink and Kopp, 2008). Melting of the ice sheets would have allowed for oxidation of dissolved Fe(II) and Mn(II) by exposing the initially covered, anoxic waters to photosynthetically-produced O_2.

However, whole-rock Pb-Pb dating of dolomitised Mooidraai carbonates by Bau et al. (1999) suggested that the Ongeluk Formation (and therefore the Hotazel Formation) may be significantly older (2394 ± 26 Ma). Moreover, age determination from detrital zircon grains of the Postmasburg group indicated a maximum age of

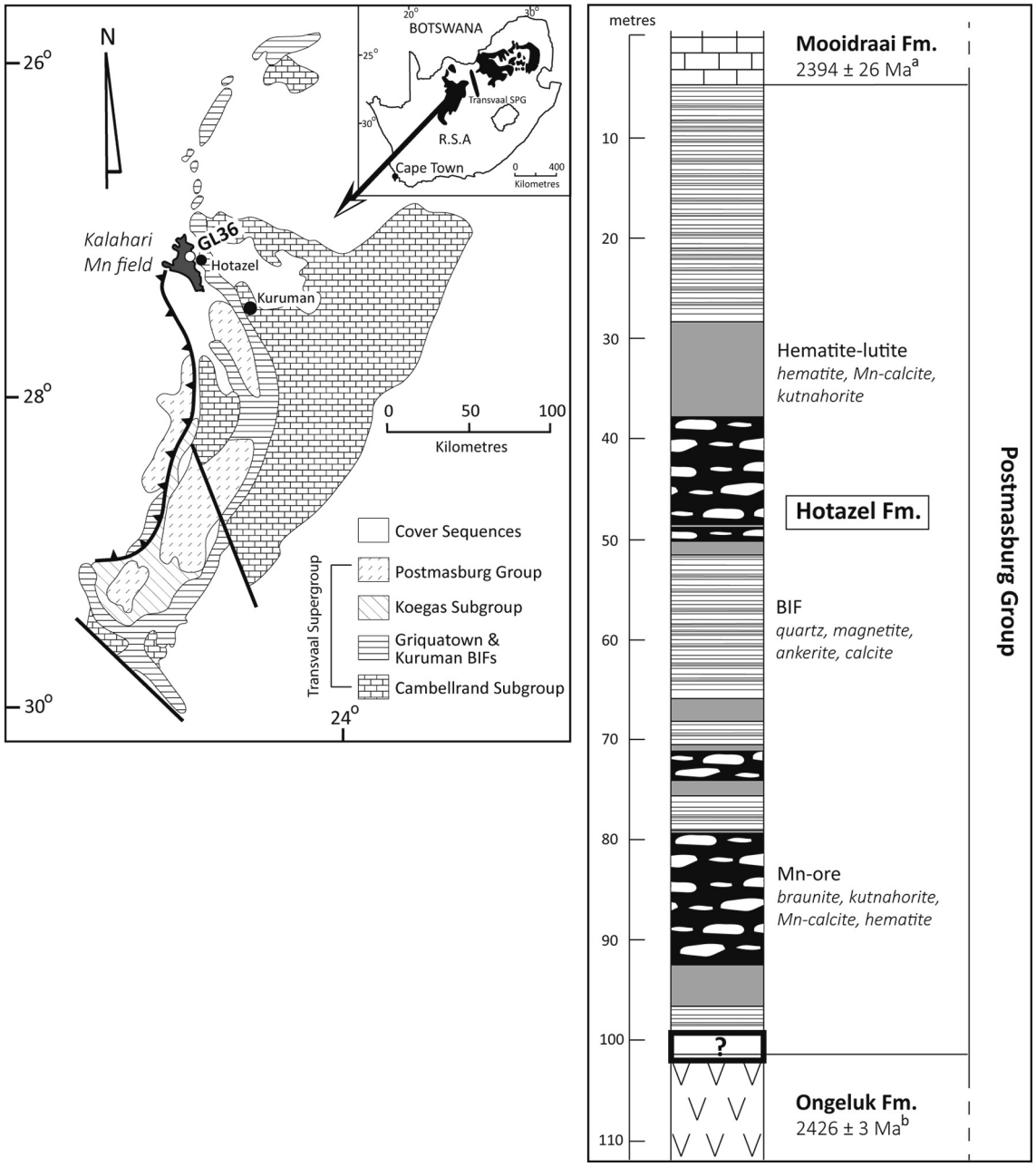

Fig. 1. A: Simplified geological map and stratigraphy of the Transvaal Supergroup in South Africa in the Griqualand West Basin (Northern Cape Province). Core GL36 was drilled at the NE part of the Kalahari manganese field (Gloria Mine). Modified from: Tsikos et al. (2010). B: Schematic log of the Hotazel Formation and its adjacent stratigraphic units, the Ongeluk Formation below and the Mooidraai Formation above, as typically developed in the Griqualand West basin. Depositional ages marked with *a* and *b* are from Bau et al. (1996) and Gumsley et al. (2017), respectively. Typical mineralogy of the three lithostratigraphic units defined in the Hotazel are from Tsikos et al. (2010). The zone indicated with the question mark forms the stratigraphic interval of interest in this study.

2436 ± 7 Ma (Moore et al., 2012). Very recent U/Pb dating of (micro) baddeleyites has yielded a much more reliable U-Pb age of 2426 ± 3 Ma for the Ongeluk volcanic sills (Gumsley et al., 2017). Consequently, deposition of the Hotazel must have taken place ca 200 Ma earlier than previously thought, immediately before or at the GOE. Elaborating on the early model of Beukes (1983) and Nel et al. (1986), Tsikos et al. (2010) therefore proposed that the cyclic character of the Hotazel, involving the characteristic succession of magnetite BIF-hematite lutite-Mn ore body, reflects transgression-regression cycles in a redox-stratified basin, in which the upper ocean layers were highly enriched in Mn(II) relative to Fe(II). They interpreted the Hotazel as being one of the terminal marine O_2 sinks in the build-up to the GOE. In contrast, Gumsley et al. (2017) placed the GOE immediately before the Hotazel Formation, at the 2426 Ma age for the Ongeluk volcanics and the near-synchronous Makganyene glacial diamictite. In doing so, they could maintain their interpretation of the Hotazel as being deposited in an oxygenated, post-glacial period, comparable to Fe and Mn deposits (Rapitan-type IFs) associated with the Neoproterozoic Snowball Earth events (Klein and Beukes, 1992).

3. Materials and methods

3.1. Rock characterisation

The Ongeluk-Hotazel transition was captured in a 3-metre-thick drill-core (GL36) interval (294–291 m) from the Kalahari Manganese Field, Northern Cape Province, South Africa (Fig. 1a). A half-core section of this interval was transported to Utrecht University, where it was

polished, photographed and visually described. Micro-X-ray fluorescence line-scanning (1 mm resolution) was carried out along the majority of the Hotazel part of the drill-core, using an EDAX Orbis PC Silicon Drift Detector Analyzer. From specific petrographic features distributed over the core, 19 thin-sections were made for more detailed examination (see Suppl. Table 1 for stratigraphic location). Mineral phases and petrographic textures were distinguished with and characterised by optical microscopy (transmitted and reflected light) and Electron microprobe analysis (JEOL JXA-8530 Field emission Electron Probe Micro Analyzer; Suppl. Materials and methods 1).

3.2. Hematite characterisation

The crystal size, morphology and cluster configurations of hematite particles from selected thin-sections in various settings were photographed and examined in detail with a FEI XL30 Field Emission Gun-Scanning Electron Microscope (FEG-SEM) and a FEI Helios Nanolab G3 Focused Ion Beam (FIB)-SEM in both BSE and SE (secondary emission) mode. Additionally, laser ablation ICP-MS (LA-ICP-MS) was applied to 8 hematite-chert-rich thin-sections distributed over the entire Hotazel-part of the drill-core with a ThermoFischer Scientific Element 2 magnetic sector ICP-MS (see Suppl. M2 for a more detailed description of the instrument setup, experimental conditions and data evaluation).

3.3. Fe isotope samples

A total of 10 samples, covering the whole stratigraphy, were selected for Fe isotope analysis (sampling location in Table 1). The 7 samples from the Hotazel Formation part were obtained from the hematite-rich chert parts with the aim to solely capture the Fe isotopic signal of hematite. Therefore, parts of the rock which looked mineralogically pure were micro-drilled or cut, yielding sample sizes of ca 200–300 mg. The Hotazel Fe isotope samples (HF 1–7) and three additional bulk-rock Ongeluk Fe isotope samples (OF 1–3) were numbered from top to bottom along the core interval. To check for the presence of Fe-bearing minerals other than hematite, X-ray diffraction (XRD) was carried out (Suppl. M3).

Pulverised samples were digested in HF-$HClO_4$-HNO_3 (following Page, 1982), including a blank, a duplicate sample (of HF7) and three certified standards (Suppl. M4). The digestions were characterised for elemental composition using Inductively Coupled Plasma – Optical Emission Spectrometry (ICP-OES, *Perkin Elmer Optima 3000* ICP-OES instrument). Afterwards, an aliquot containing between 220 and 430 µg Fe was purified using the protocol of Williams et al. (2004). The Fe isotope ratio measurements were done in medium high mass resolution mode on a ThermoFinnigan Neptune multicollector inductively coupled plasma mass spectrometer (MC-ICP-MS) at the Helmholtz Laboratory for the Geochemistry of the Earth Surface at GFZ Potsdam using a ThermoFinnigan stable introduction system (SIS) with a PFA-ST Nebulizer (nominal uptake of 100 µL/min), a concentration of ca. 5 ppm Fe in 0.3 M HNO3 and standard-sample-standard bracketing to correct for instrumental mass bias. Accordingly $\delta^{56}Fe$ is reported as:

$$\delta^{56}Fe_{sample} = [{}^{56}Fe/{}^{54}Fe_{unbracketed\ sample}/({}^{1}/_{2}*({}^{56}Fe/{}^{54}Fe_{IRMM\text{-}014\ before} + {}^{56}Fe/{}^{54}Fe_{IRMM\text{-}014\ after})) - 1] * 1000\ (‰);$$

The data acceptance criteria of Schoenberg and Von Blanckenburg (2005) were used. The typical overall uncertainty was estimated to be 0.1‰. Quality control samples show agreement with their reference values (Suppl. M4).

Table 1
IRMM-014-normalised $\delta^{56}Fe$ compositions and chemistry of hematite-chert from the Hotazel (HF1-7) and of bulk-rock Ongeluk Formation (OF1-3), along with the sampling depth. HF7a and b are duplicate samples. The external 2 S.D. uncertainty for $\delta^{56}Fe$ is established at ± 0.1‰. OF1-3 additionally contain traces of K, P and Ti (Suppl. T10).

Sample	Depth (m)	$\delta^{56}Fe$ ‰	Fe_2O_3 wt%	MgO wt%	MnO wt%	Al_2O_3 wt%	CaO wt%	SiO_2 + rest wt%
HF1	291.259	−0.26	10.7	0.2	0.0	0.1	0.1	88.9
HF2	291.625	−0.31	11.0	0.3	0.0	0.3	0.4	88.0
HF3	291.837	−0.38	5.9	0.5	0.0	0.1	0.2	93.3
HF4	291.937	−0.49	5.6	0.2	0.0	0.5	0.1	93.6
HF5	292.322	−1.07	3.1	1.4	0.0	0.8	0.0	94.7
HF6	292.900	−0.93	6.0	0.3	0.1	0.1	1.4	92.1
HF7a	293.425	−0.50	24.9	0.4	0.1	0.2	1.1	73.3
HF7b	293.425	−0.50	23.7	0.4	0.1	0.2	1.0	74.6
OF1	293.854	−0.70	22.6	9.5	0.4	12.9	2.1	52.5
OF2	294.000	−0.73	17.2	10.2	0.5	11.2	2.0	59.1
OF3	294.137	−0.65	22.9	9.9	0.5	15.6	5.0	46.1

4. Results

4.1. Lithostratigraphy

The GL36 drill-core section (Fig. 2) captures the top 35 cm of the Ongeluk Formation volcanics and the basal 2.8 m of the Hotazel Formation. The Ongeluk part consists of uniform, dark-green volcanic rock and is conformably overlain by dark red lutite from the Hotazel. The rocks resemble the “transitional lutitic lithologies” identified at the contacts between the BIF and manganese ore bodies higher up in the Hotazel stratigraphy (Tsikos et al., 2010). The lutite contains three hematite-rich intervals (hematite-lutite) alternated with three clay mineral-rich intervals (mudstone), separated by chaotically bedded intervals of mixed composition (transition zone). At the top of the core section, laminated mudstone changes into a microbanded BIF.

4.2. Sedimentology and petrography

In the following sections the different lithostratigraphic units defined in the drill-core (Fig. 2) are briefly described with respect to their sedimentary structures, petrographic textures and mineralogical composition. Descriptions of the textural and mineralogical features from all 19 thin-sections are listed in Supplementary Results Table 1; the chemical compositions of all minerals identified with EMPA are listed in Suppl. T2–T4.

4.2.1. Ongeluk formation

The Ongeluk volcanics exclusively consist of secondary minerals and only a relict porphyritic texture is recognisable (Fig. 3). The rock’s dark-green colour can be attributed to the abundance of secondary chlorite (chamosite or clinochlore). Chlorite minerals occur as anhedral aggregates replacing the originally fine-grained (≪1 mm) groundmass minerals and as pseudomorphs after a euhedral igneous precursor (clinopyroxene according to Schütte, 1992). Feldspar phenocrysts (< 1 µm up to 2 mm long) contain numerous small gaps filled with chlorite or quartz that presumably replaced plagioclase (Schütte, 1992). Secondary titanite is present as minute aggregates at the edges of chlorite and quartz patches, and occasionally, secondary calcite occurs as irregularly shaped patches cutting across the chlorites and feldspars, or filling up small secondary veins.

4.2.2. Contact between the Ongeluk and Hotazel formation

The Ongeluk volcanics have a different fabric close to the contact with the overlying Hotazel (Fig. 3b-d). The rock consists almost completely of chlorite, and no feldspars are found here. Optical microscopy reveals several opaque veins that are branching from the Ongeluk towards the contact (Fig. 3b). The veins are typically 100–400 µm wide, consist mainly of chlorite with traces of calcite and titanite and are rimmed by radiating, microplaty hematite (Fig. 3d). Minute dendritic chlorite crystals grow out of these veins, perpendicular to the propagation direction of the veins. At the Ongeluk-Hotazel contact, chlorite forms a uniform layer of vertically directed needles. Directly above the contact (i.e. in the Hotazel) detrital chlorite grains were found, containing traces of barite, chalcopyrite and galena (Fig. 3c).

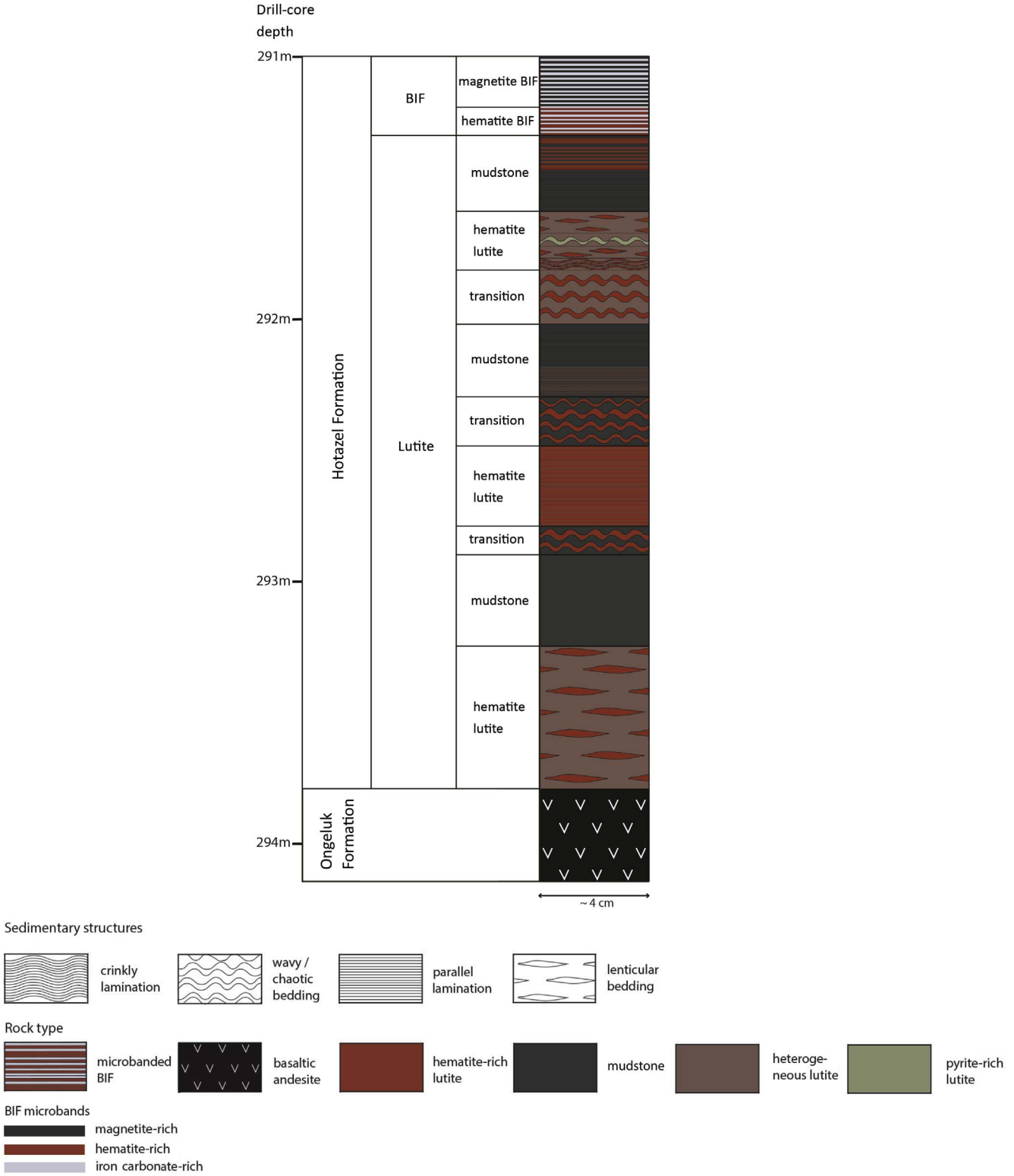

Fig. 2. Stratigraphic chart of drill-core GL36 at depth interval 294.14–291.00 m. The lithology pictured in the stratigraphic chart is based on two characteristics: i) sedimentary structures and ii) mineralogy in combination with rock type.

4.2.3. Hotazel lutite

4.2.3.1. Hematite-lutite. The characteristically deep-red colour of the hematite-lutite intervals arises from the prevalence of minute hematite particles ("dusty hematite") that are finely disseminated within a microcrystalline quartz (chert) groundmass. The lowermost interval is characterised by elongated, bright-red lenses composed of almost pure hematite-chert, surrounded by a more brown-purplish to dark grey matrix representing a mineralogically more heterogeneous composition. Specifically, the dark grey colour (and metallic lustre) results from the predominance of large (up to 100 μm) and well-crystallised magnetite rhombohedra. They occur as randomly distributed crystals in the matrix or as crystals grouped together to form microbands, and frequently overgrow the other minerals. Further, the heterogeneous matrix rock is more clastic-textured, especially in the

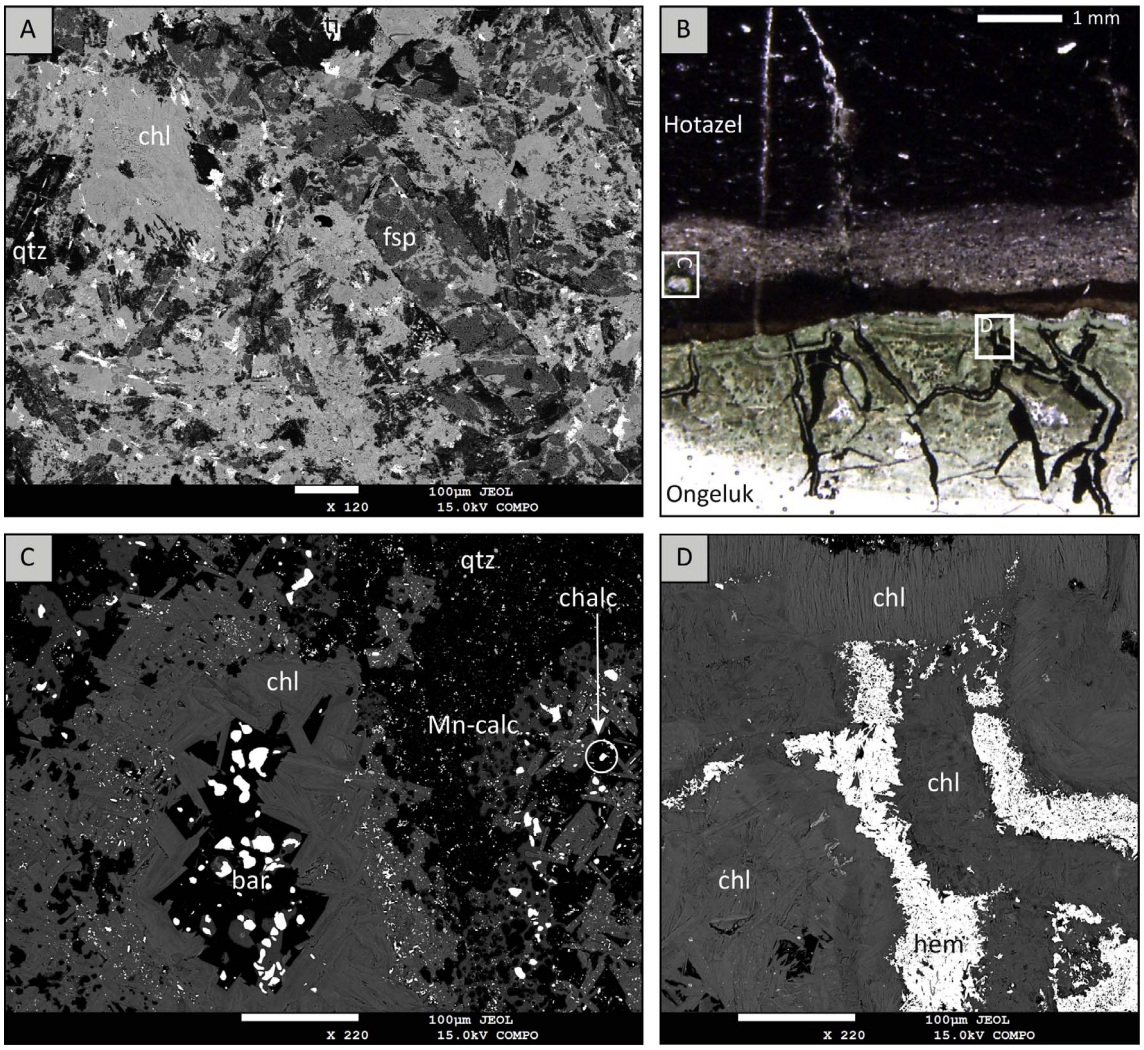

Fig. 3. Images representative of the various minerals and textures found in the upper part of the Ongeluk lava and near the contact with the overlying Hotazel. A: BSE image of the Ongeluk lava, showing feldspar (fsp) and chlorite (chl) pseudomorphs with intergrown anhedral patches of chlorite, titanite (ti) and quartz (qtz). B: Plane-polarised light image the contact between the Ongeluk and Hotazel. C: Inset of B. BSE image of a detrital grain in the lowermost Hotazel, containing barite (bar) and chalcopyrite (chalc) associated with Mn-calcite (Mn-calc) and surrounded by a rim of detrital chlorite. D: Inset of B. BSE image showing massive, microplaty (ca 5 µm) hematite (hem) rimming the branching structures, which are filled-in with and surrounded by chlorite. Note the layer of uniformly aligned chlorite needles at the contact with the Hotazel.

lowermost part nearest to the Ongeluk. Stilpnomelane, minnesotaite (ferrroan talc) and minor chlorite are typically concentrated in these grains, where chlorite is commonly overgrown by stilpnomelane, which is in turn replaced by minnesotaite. In addition, minnesotaite is often associated with or seen to overgrow manganoan calcite (Mn-calcite), which contains ca 3.7 wt% of Mn (Suppl. T2). The large, anhedral Mn-calcite crystals cover a substantial area of the lowermost Hotazel, though their contribution to the rock's bulk Mn content (< 1 wt%) is minor (Suppl. F3). The crystals contain many rounded gaps surrounding the groundmass chert (Fig. 4a) or locally barite grains (Fig. 3c). In the middle part of the hematite-lutite, minor pyrite is present in the form of large, spherulitic nodules (Fig. 4b), indicating early diagenetic microbial sulphate reduction (Raiswell, 1982; Bekker et al., 2004).

The second hematite-lutite interval is devoid of any clastic textures or lens-shaped inclusions and comprises horizontally bedded layers of dark red jasper that are gradually alternated with darker, more magnetite-rich chert bands. Rarely, small aggregates of cubic pyrite occur within these magnetite-rich layers. The sedimentary textures of the third interval resemble those of the first, but at the base a short interval of crinkly lamination occurs. It has a characteristic curved-wrinkled appearance and typically consists of alternating mono-mineralic lamina (50 µm–1 mm thick) composed of hematite, minnesotaite and stilpnomelane, and occasionally of magnetite or chlorite (Fig. 4c). The middle part of the third hematite-lutite is interrupted by a thin, chaotically bedded layer dominated by cubic pyrite and magnetite.

4.2.3.2. Transition zone. The transitional intervals consist of irregularly shaped bulges of jasper intermingled with dark green nodular (chlorite) mudstone (in case of the first and second interval) or with heterogeneous lutite (in the third interval). The jasper bulges vary in colour from bright red to dark purple, reflecting various contributions of magnetite, stilpnomelane, minnesotaite and Mn-calcite impurities. Their wavy appearance suggests they are load casts formed during soft-sediment deformation (SSD) rather than granular features. However, the third transitional interval additionally contains several heterogeneous clasts of detrital origin, forming "chaotic intraformational breccia" (Simonson, 1985 and references therein).

4.2.3.3. Mudstone. The dark greenish-grey coloured mudstone intervals are significantly richer in magnetite, chlorite and stilpnomelane and poorer in hematite than the hematite-lutites; this is also highlighted by their significantly higher Al concentration (Suppl. F3). The first mudstone interval displays no obvious lamination and is largely composed of chlorite nodules (0.1–1 mm in diameter). The

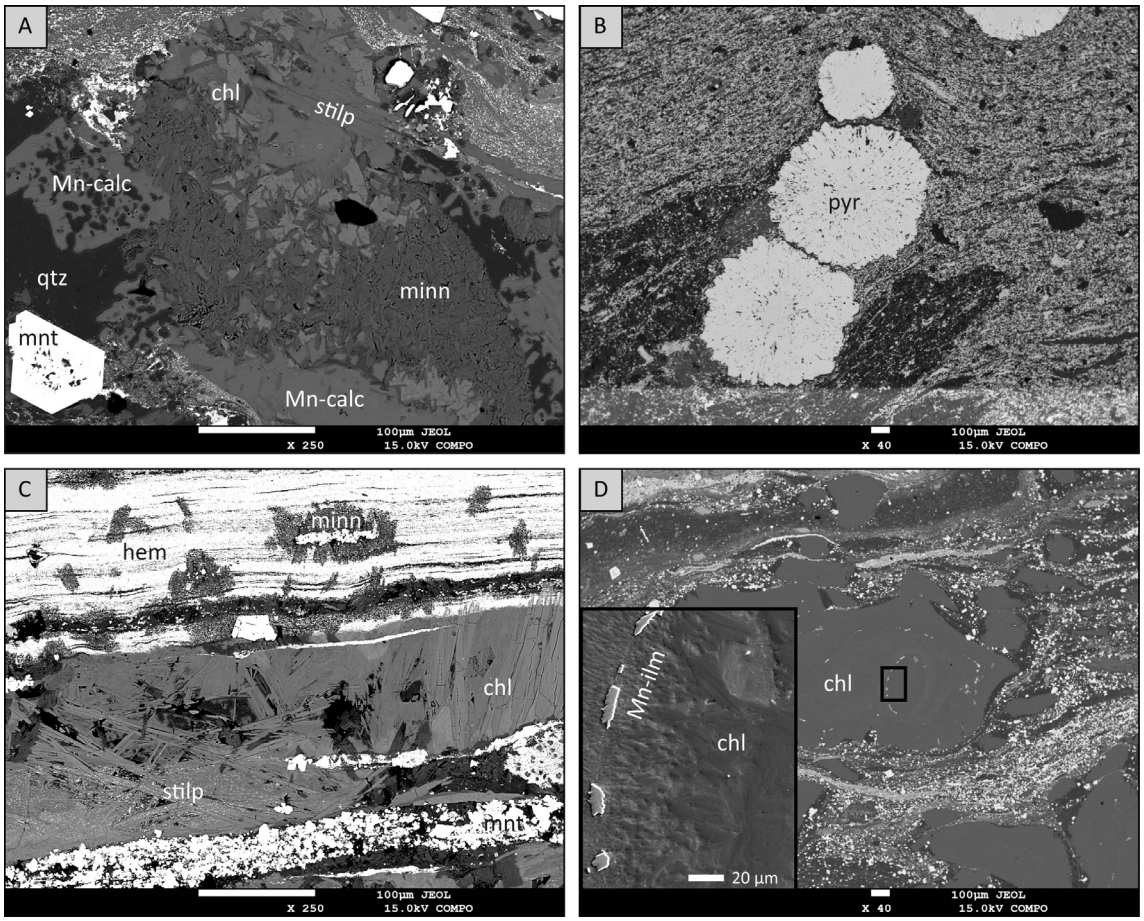

Fig. 4. BSE images representative of the various minerals and textures found in the Hotazel lutite. A: Granular texture consisting of minnesotaite (minn), chlorite, stilpnomelane (stilp) and Mn-calcite, surrounded by chert and randomly scattered magnetite (mnt). Parts of the Mn-calcite sheets are full of holes that are filled in by chert. B: Pyrite (pyr) spherulites within heterogeneous hematite-chert matrix. C: Crinkly laminated sequence of mono-mineralic bands composed of magnetite, well-crystallised stilpnomelane, chlorite and minnesotaite, and covered by < 1 µm hematite. D: Chlorite spherulites within a mudstone matrix. The inset represents a detailed surface relief (SE) image showing the radial orientation of the chlorite crystals and a concentric rim of Mn-ilmenite (Mn-ilm).

internal structure of the nodules varies: chlorite fibres occur either as randomly oriented clusters or in radial orientation producing spherulites (Fig. 4d). They regularly display concentric growth rims along which manganoan ilmenite (Mn-ilmenite) has formed (inset Fig. 5d). The chlorite minerals are high in Al compared to stilpnomelane, and their physical characteristics and chemistry are quite similar to those of the Ongeluk chlorites, though the latter average Al content is 5.6 wt% higher (Suppl. T2). In the Hotazel this Al has presumably been incorporated in the crystal lattice of stilpnomelane overgrowths. Mn-ilmenite and euhedral F-apatite are accessory phases that are omnipresent in the Hotazel rocks, but typically occur in the mudstones and clastic-textured parts. F-apatite also particularly occurs in pyrite- and minnesotaite-rich areas.

The second mudstone interval resembles the first, except that the lower part has a more brownish-red rather than greenish tint, reflecting a relatively larger contribution of hematite. The third mudstone is devoid of chlorite nodules and evolves from a parallel-laminated, dark grey mudstone at the base into a banded mudstone of alternating brownish-red (hematite-rich) and dark grey lamina (hematite-poor), marking the change from a lutite into a BIF. Chlorite is still present, albeit in far lower volumes and as small patches scattered within the matrix rather than in nodular form.

4.2.3.4. Hotazel BIF. The Hotazel BIF part comprises rhythmic alternations of Fe-rich and Fe-poor bands (i.e. microbands), which are typically composed of magnetite and chert-dolomite-stilpnomelane, respectively (Fig. 5a). Chlorite is virtually absent. Dolomite crystals (10–100 µm) are relatively poor in Mg (11.2–17 wt%), which is substituted by Mn (8–11 wt%) and Fe (3.8–9 wt%), and are therefore classified as ferromanganoan dolomite (Fe Mn-dolomite). Rhomb-shaped crystals show chemical zoning: the crystal core has a lower Fe/(Fe + Mg + Mn) ratio compared to the outer rim (Suppl. T2). The inner part of the rhombohedral dolomites contains many chert inclusions that have been enclosed during carbonate crystal growth (Fig. 5b; Sun et al., 2015; Haugaard et al., 2016).

In the lower part of the BIF, a considerable portion of the Fe-rich layers are composed of jasper instead of magnetite; they only contain a few discontinuous magnetite laminae. The jasper layers consist of very fine-grained hematite and Fe silicate (< 1 µm); thin (10–150 µm) beds of densely packed hematite and Fe silicate define relict primary bedding in chert. The very small grainsize of the Fe silicates prevented their composition analysis by EMPA. However, considering their striking similarities (Figs. 5c, 6c) with the iron silicate nanoplates (50 nm–1 µm in length) identified with high-resolution TEM imaging by Rasmussen et al. (2017), we tentatively classify them as greenalite.

In these hematite- and greenalite-rich layers, gaps in the dolomite rhombs are occasionally occupied by residual hematite-greenalite clusters. In anhedral carbonates these hollows are filled in by secondary magnetite grains (Fig. 5c). Further, anhedral dolomite is found attached to or overlying spongy hematite intergrowths (inset Fig. 5c and Suppl. F2). Figs. 5c-d, 6c and Suppl. F2 display a variety of observed textures that reveal the different stages of overgrowth of magnetite from

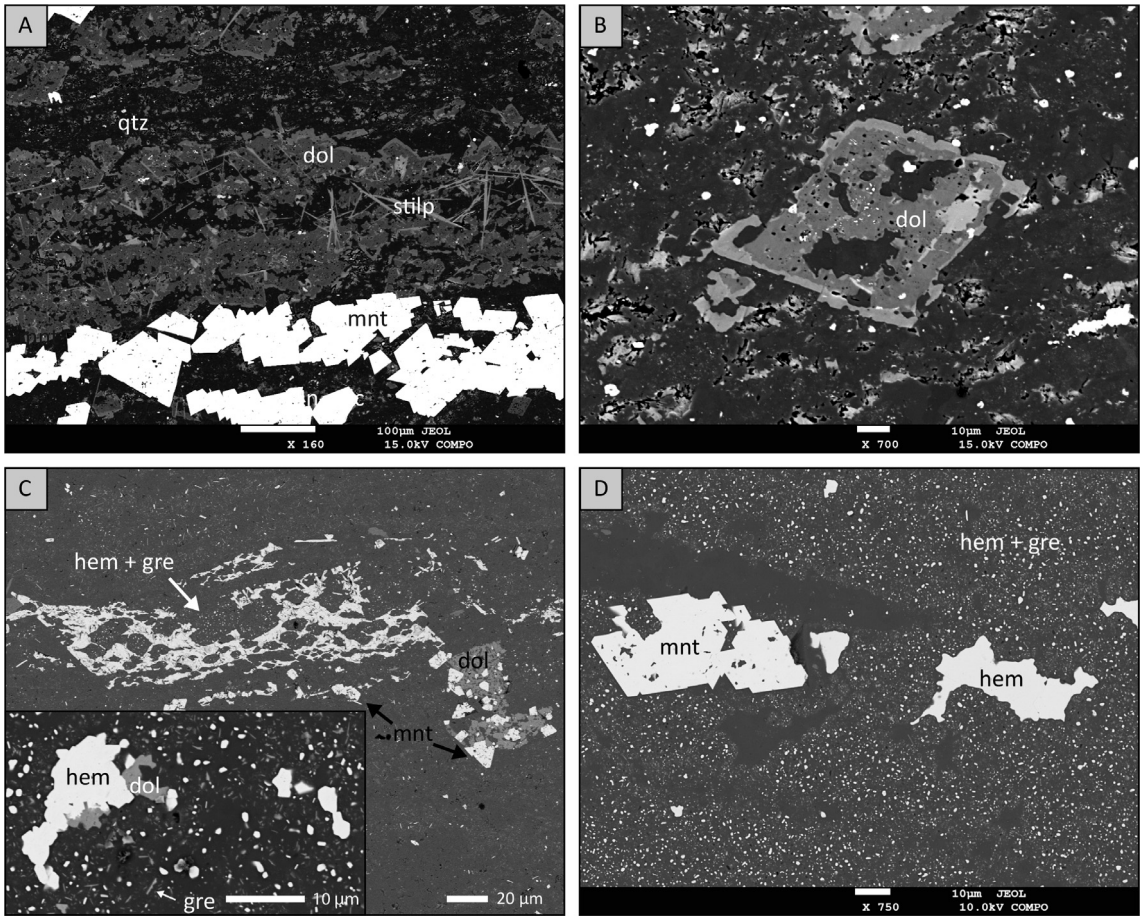

Fig. 5. BSE images showing details of the Hotazel BIF. A: Microbands of euhedral magnetite and Fe Mn-dolomite (dol), overlain by stilpnomelane needles, within a chert matrix. B: Close-up of an Fe Mn-dolomite rhomb showing chemical zoning. Its crystal core contains numerous chert inclusions. C: Middle: framework of anhedral magnetites enveloping microspheroidal chert with hematite and greenalite inclusions. Right: anhedral dolomite with numerous chert inclusions, of which several have been occupied by magnetite. *Inset*: anhedral dolomite growing from a spongy hematite intergrowth, within a matrix of floating hematite and greenalite particles (< 1 µm). D: Spongy hematite intergrowth and euhedral magnetite overgrowing hematite-greenalite microspheroids.

hematite, i.e. small spongy hematite intergrowths; clusters of hematite-greenalite encapsulated by spongy hematite; or by anhedral magnetite; magnetite 'ghost textures' (Han, 1978); and euhedral magnetite.

4.3. Characterisation of hematite-chert

4.3.1. Hematite crystal size, habit and configuration

In the various jasper sections of the Hotazel, hematite occurs as sub-rounded to hexagonal plates with a diameter ranging from 100 to 800 nm (Fig. 6). In the lutitic jasper lenses or bulges of the Hotazel lutite part, the crystals are configured in concentric networks, forming trains around spherical globules of chert (Fig. 6a). In the crinkly laminated interval, the individual hematite crystals are preferentially aligned to the horizontal lamination (Fig. 6b). In the hematite-rich BIF layers at the top of the drill-core, 'floating' hematite and greenalite particles (< 1 µm) are concentrated in spheroids (typically 10–20 µm), enclosed by rims of chert (Fig. 6c-d). The term "floating" here means that the individual crystals rarely touch. The spheroids bear an obvious resemblance to the greenalite polygons that were interpreted to represent shrinkage structures during silica recrystallization (Rasmussen et al., 2017).

Spongy hematite agglomerates (> 1 µm) occur locally in the surrounding interpolygon areas (around the spheroids), or they have completely overgrown these hematite-greenalite microspheroids. In the mudstones and in more heterogeneous parts (where hematite is a minor mineral constituent), hematite is present as randomly and/or radially oriented, rod-like crystals (typically 5 µm in length), scattered through the matrix or forming small clusters (Fig. 6e). Locally, hematite has overgrown stilpnomelane or chlorite needles (Fig. 6f). In the veins at the contact with the Ongeluk volcanics massive aggregates of radiating, microplaty hematite (> 10 µm in length) have developed (Fig. 3d).

4.3.2. Trace and rare-earth element geochemistry

Laser ablation ICP-MS results from multiple thin-sections along the Hotazel stratigraphy yield distinct rare-earth element and Yttrium (REE + Y) distribution patterns for hematite-chert (Fig. 7a; thin-section location is given in Suppl. T1). All hematite-chert samples have depleted REE + Y abundances compared to PAAS (Pourmand et al., 2012) and contain little detrital material, as indicated by their low Zr, Al and Sc concentrations. When compared to bulk-rock samples of Neoarchean/Paleoproterozoic IFs (e.g. Bau et al., 1997; Derry and Jacobsen, 1990; Bolhar et al., 2004; Planavsky et al., 2010), hematite-chert shows a depletion in the light REE (LREE) relative to the heavy REE (HREE), insignificant to large positive Eu anomalies and superchondritic Y/Ho values (Suppl. T8). Furthermore, none of the samples has a true positive La or negative Ce anomaly (Suppl. F5) as defined by Bau and Dulski (1996).

The sample obtained from a hematite-rich BIF layer (thin-section 2) is conspicuously more LREE-depleted than the other hematite-chert samples from the Hotazel lutite part (thin-sections 6, 8, 9, 11, 13, 14 and 16). Its average $(Pr/Yb)_{SN}$ (ca. 0.03) is more than a factor 10 lower than that of lutite hematite-chert (ca. 0.38) and even lies below that of relatively strongly LREE depleted modern open-ocean seawater (e.g. 0.13 as in Bau et al., 1996; Fig. 7b). Although this BIF layer is the only

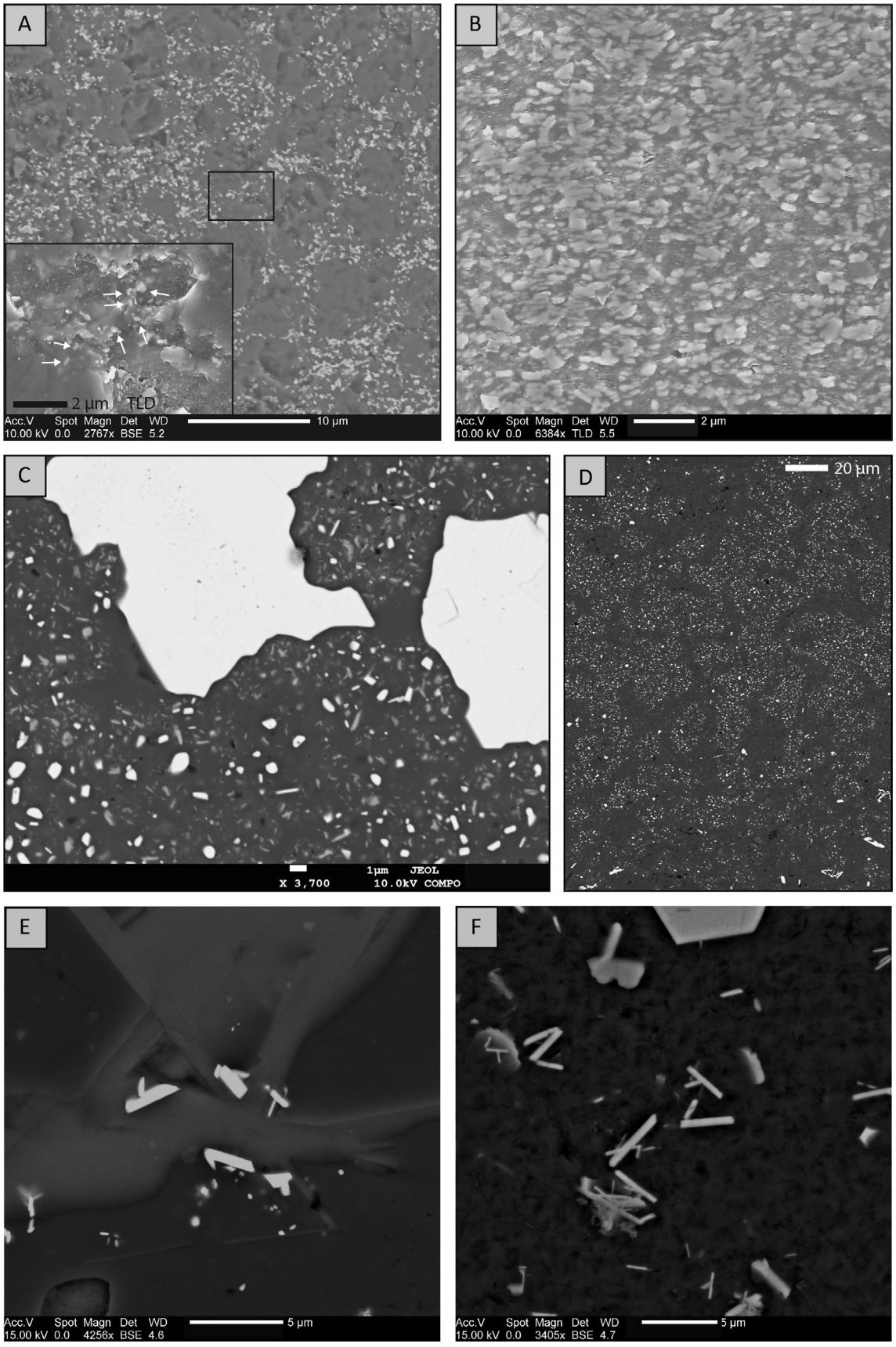

Fig. 6. BSE and SE images showing hematite configuration, size and crystal habit in the hematite-rich chert (A-D) and hematite-poor (E-F) sections of the Hotazel. A: BSE image (and SE in inset) of a jasper lens. Sub-rounded to elongate (100–200 nm) hematite particles are forming concentric networks around chert globules. B: SE image of a hematite-rich crinkly laminated layer showing bedding-parallel alignment of sub-rounded to hexagonal hematite plates. C: BSE image of a hematite-rich BIF layer. Spongy hematite aggregates have grown around hematite- and greenalite-rich chert polygons. D: BSE image of a BIF layer showing hematite-greenalite microspheroidal or -polygonal structures. E: Stilpnomelane fibres are replaced by long (> 1 µm) hematite laths. F: Rod-like hematite particles (> 1 µm) are scattered randomly within a chlorite nodule.

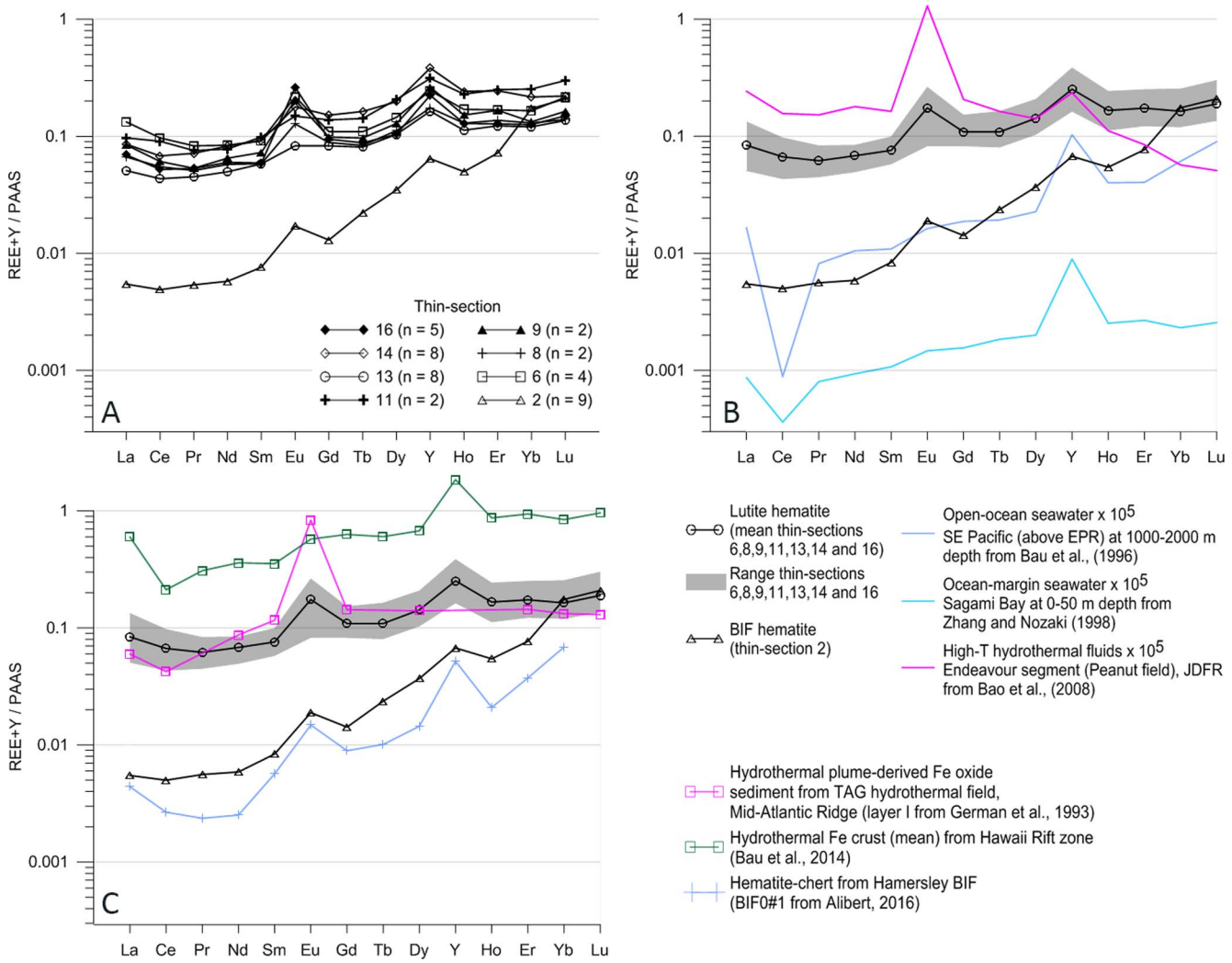

Fig. 7. Rare-earth element and Yttrium (REE + Y) diagrams (log-scale) normalised to Post-Archean Average Shale (PAAS). A: Average REE + Y distribution patterns per thin-section. B: Comparison of the two distinct REE + Y profile groups from this study, i.e. BIF and lutite jasper (see text), to representative REE + Y patterns of the modern ocean and hydrothermal fluids. C: Comparison to REE + Y profiles of modern hydrothermal Fe-rich deposits (bulk-rock data) and of BIF hematite-chert (laser ablation ICP-MS data). (See above-mentioned references for further information.)

sample that contains (abundant) greenalite nanoparticles (hematite-greenalite-chert), its profile does not match with LA-ICP-MS REE + Y patterns for greenalite from Hamersley BIFs (Alibert, 2016), which have a higher total REE + Y and $(Pr/Yb)_{SN}$ composition. Instead, it bears much more resemblance to the REE + Y pattern of Hamersley BIF hematite-chert (Fig. 7c). The $(Pr/Yb)_{SN}$ ratio of lutite hematite-chert compares well to that of shallow ocean-margin seawater (i.e. 0.35; Zhang and Nozaki, 1998) and to that of bulk-rock hydrothermal Fe crust specimens from the Hawaii Rift zone (Bau et al., 2014; Fig. 7c). However, the latter patterns lack a positive Eu anomaly, which becomes apparent only for a higher temperature (> 250 °C) hydrothermal source (e.g. German et al., 1993).

4.4. Fe isotope samples

XRD results (Suppl. T9) confirm that samples HF1-7 largely consist of quartz, and secondly hematite. Minor contributions of other minerals are present as well, but their spectrum peaks hardly stand out of the background level and thus could not be labelled with certainty as a particular mineral. Bulk-rock ICP-OES major and trace element data of HF1-7 and OF1-3 are listed in Suppl. T10; calculated major oxide weight fractions are summarised in Table 1. The average Fe_2O_3 content of HF7 (ca 23.9–24.7 wt%) is considerably higher than for the other samples. HF5 contains very little Fe_2O_3 (ca 3.1 wt%) and is relatively rich in MgO and Al_2O_3, which presumably reflects an Fe silicate contribution. HF6 contains a substantial amount of CaO relative to Fe_2O_3, possibly hosted in Mn-calcite and/or Fe carbonate. MgO, Al_2O_3 and CaO contributions similarly exist in HF3-4, albeit in lower volumes. Based on XRD and ICP-OES data, HF7 is evidently the richest in hematite(-chert), followed by HF1 and next HF2. Yet, petrographic observations have revealed the abundance of greenalite nanoparticles in HF1.

The $\delta^{56}Fe$ values of the hematite-chert samples (Table 1) range from −0.26‰ to −1.07‰, which is up to 2‰ higher than those of the transitional hematite-lutite samples (from −1.52 to −2.40‰) reported higher up in the Hotazel stratigraphy (Tsikos et al., 2010). The $\delta^{56}Fe$ of the Ongeluk samples lies in between −0.65‰ and −0.73‰, which is significantly lower than the near-zero values (± 0.05‰) for most igneous rocks (Beard et al., 2003; Poitrasson et al., 2004). A noticeable stratigraphic trend is seen (Fig. 8) of decreasing $\delta^{56}Fe$ from HF7 to HF5 followed by a continuous increase in $\delta^{56}Fe$ to the top of the section. The lowest $\delta^{56}Fe$ values of samples HF5 and HF6 coincide with a relatively low Fe_2O_3 content.

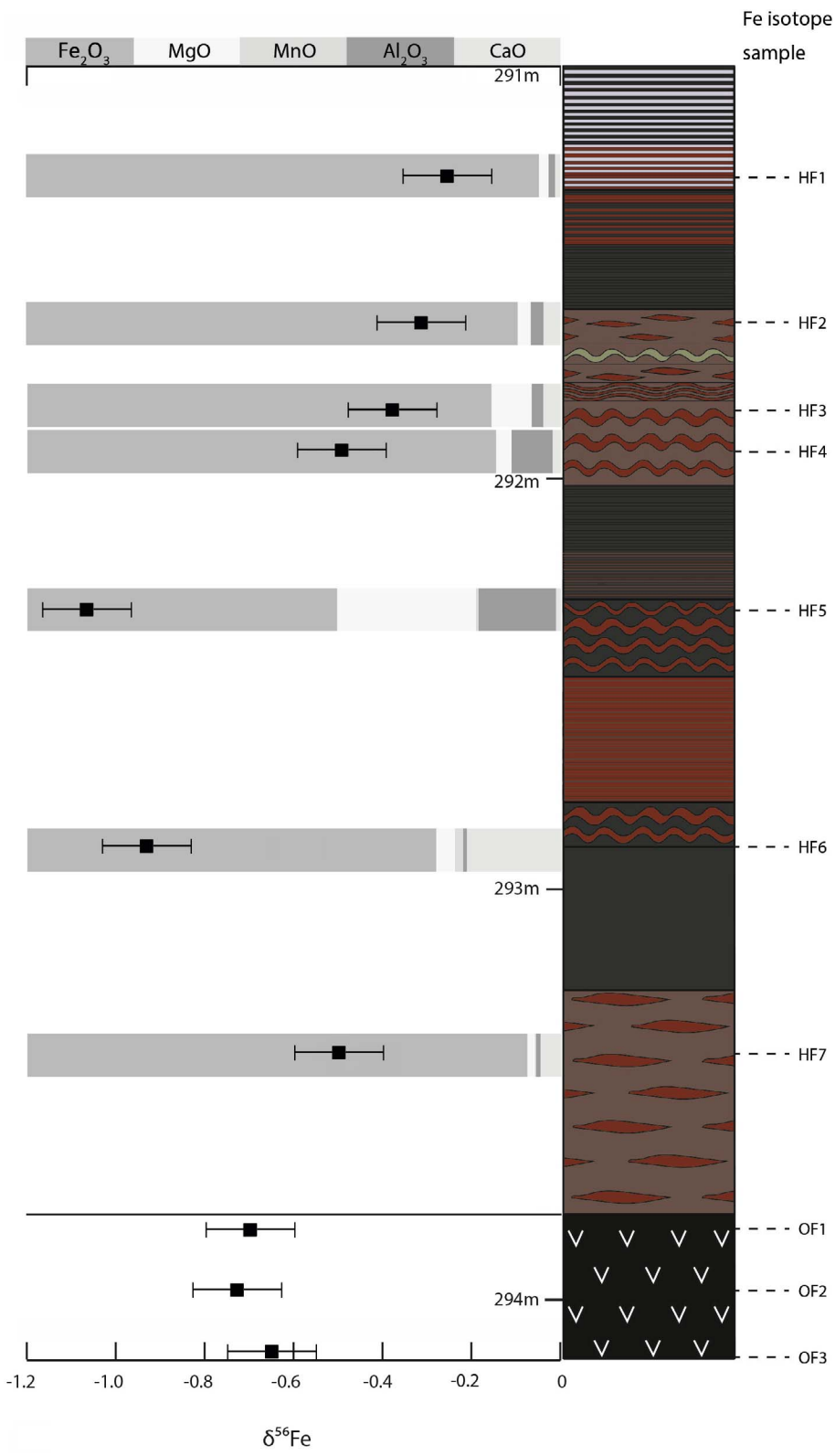

Fig. 8. Overview of $\delta^{56}Fe$ results of samples from the Hotazel (HF1-7) and Ongeluk (OF1-3) Formation versus stratigraphic depth, combined with their major chemical composition (relative oxide weight %). The error bars indicate the ± 0.1‰ external uncertainty limits.

5. Discussion

5.1. Subaqueous extrusion and hydrothermal alteration of Ongeluk volcanics

The observed porphyritic texture, very fine-grained matrix (crystal sizes ≪ 1 mm) and conformable contact of the Ongeluk volcanics with the overlying marine precipitates of the Hotazelprovide arguments for subaqueous extrusion. This is concomitant with the widespread occurrence of pillow lavas and hyaloclastites elsewhere within the Ongeluk Formation. (Grobler and Botha, 1976; Schütte, 1992; Cornell and Schütte, 1995; Cornell et al., 1996). The characteristic hematite veins that appear at the Ongeluk-Hotazel contact and subsequently branch downward into the Ongeluk likely represent pathways through which

seawater interacted with the lava. The minute dendritic textures that are directed outward from the veins may reflect supercooling, resulting from the interaction between relatively cool seawater with hot lava. The thick rim of microplaty hematite might indicate a reaction with oxygen-bearing surface waters, but because it is secondary (Section 5.2.2) the timing of its formation and hence its significance is unclear.

Seafloor and/or hydrothermal alteration of the upper Ongeluk (as was previously reported by Schütte, 1992; Cornell and Schütte, 1995; Cornell et al., 1996) has had a major effect on its original igneous composition, as demonstrated by the omnipresence of chlorite and feldspar pseudomorphs and other secondary mineral intergrowths. The traces of barite, chalcopyrite and galena included in detrital grains directly above the contact (Fig. 3c) were presumably derived from reworking of laterally exposed hydrothermal vents: this mineral assemblage is typical for modern, low T (< 350 °C) hydrothermal chimneys (Haymon and Kastner, 1981). The chlorite minerals, which these detrital grains are largely made up of, are very similar in appearance and chemistry to those found in the chlorite-altered Ongeluk volcanics. By implication, hydrothermal alteration of Ongeluk lava must have started prior to accumulation of sediments (such as weathered Ongeluk volcanic material) onto the seafloor, and thus must have been roughly coeval with its subaqueous extrusion.

5.2. Hotazel depositional environment

5.2.1. Detrital vs hydrogenous sediments

The Hotazel strata broadly record a facies change from a relatively shallow marine environment (continental shelf) towards a deeper marine setting. The relict starved wave ripples (lenticular bedding) and the microbial crinkly lamination in the lutitic part are clear indicators of above fair-weather wave base conditions (e.g. Pettijohn, 1975; Simonson, 1985; Beukes and Gutzmer, 2008), while the finely bedded BIF at the top of the studied core section implies a more distal setting (Beukes and Gutzmer, 2008). Like the BIF part, the fine-grained hematite-lutite intervals primarily represent in situ chemical precipitation, whereas the recurrence of heterogeneous, clastic-textured intervals and Al-rich mudstones reflects reworking of Fe-rich shelf deposits and episodes of distal volcanogenic sediment input, respectively.

The predominance of chlorite spherulites in the mudstone intervals suggests these are chiefly composed of Ongeluk-derived volcanogenic sediment, the nodules representing former volcanic glass spherules or refilled vesicles that were chloritised by hydrothermal alteration and subsequently re-deposited onto the seafloor. The replacement of chlorite spherulites by chains of euhedral Mn-ilmenite (Fig. 4d) further suggests the nodules additionally contained a Ti-bearing precursor mineral, presumably titanite from the Ongeluk volcanics. Hence, the mudstones could represent direct pyroclastic fall or resedimented syneruptive pyroclastic fall deposits associated with active episodes of Ongeluk volcanism. Alternatively, the mudstone intervals may represent post-depositional reworking and re-sedimentation of Ongeluk volcaniclastics via density currents induced by sea level fluctuations (e.g. Krapež et al., 2003). The chaotic bedding of the transition intervals might be in support of a density current origin, although we estimate the majority of the wavy structures to primarily reflect soft-sediment deformation due to density differences, rather than far-ranging lateral sediment transport. Irrespective of the sedimentation mechanism, the contribution of volcanogenic material (i.e. chlorite) vanishes as we approach the Hotazel BIF part, signifying a spatial and temporal shift towards the deep-marine realm.

5.2.2. Primary origin of hematite and greenalite

The petrographic results from the Hotazel IF emphasise the limited effect of post-depositional alteration. The overall mineralogy, preserved primary textures and paragenetic relationships imply early sediment diagenesis to very low-grade regional metamorphism, in line with temperatures estimated for the Asbestos Hills BIFs in the Griqualand West basin (100–150 °C Miyano and Beukes, 1984; Klein, 2005). No indications for secondary processes such as hydrothermal alteration or supergene oxidation are found.

We consider the finely disseminated hematite particles (< 1 μm) from the various jasper lenses, bulges or layers within the Hotazel (i.e. 'dusty' hematite) to be a very early, "primary" mineral phase, because (1) they are very fine-grained; (2) they do not overgrow any other Fe-bearing minerals; (3) they occur 'floating' in the chert matrix, which implies that they were formed prior to silica cementation; and (4) they define primary sedimentary bedding (at least in the BIF part). Based on their sub-rounded to hexagonal crystal form and size (100–800 nm), these hematite crystals are classified here as type II hematite (following Sun and Li, 2017). Type II hematite is thought to be a diagenetic overprint of ultrafine (3–5 nm) hematite particles (e.g. Ahn and Buseck, 1990; Sun et al., 2015). In turn, these are likely to be dehydration products of tiny ferric oxyhydroxide colloids (e.g. Ahn and Buseck, 1990; Morris, 1993; Bekker et al., 2010) that where formed in the water column via oxidation of Fe(II) with cyanobacterial O_2 (e.g. Klein and Beukes, 1989) or anaerobically/micro-aerobically by enzymatic Fe(II) oxidation (e.g. Widdel et al., 1993; Konhauser et al., 2002; Kappler et al., 2005). Coarsening of the ultrafine (3–5 nm) hematite particles was presumably promoted by structural waters that were released from the surrounding silica during burial lithification, i.e. during transformation from amorphous silica to quartz (e.g. Meng et al., 2009; Sun et al., 2015). However, this coarser hematite would have retained the original Fe signal of the seawater, and is therefore considered primary.

Another argument for a primary origin of hematite (< 1 μm) is the preferential crystal alignment of hematite particles in the microlaminae of the crinkly laminated interval (Fig. 6b). The crinkly character of the lamination, the clay mineral enrichment (i.e. stilpnomelane, minnesotaite and chlorite) and the lamina-specific distribution of the minerals are indicative of microbial mats (Schieber, 1999). The specific ordering of the hematite particles in microlamina might therefore signify oxidation and precipitation of aqueous Fe(II) and ferric oxyhydroxide particles, respectively, promoted by a microbial community.

In the Hotazel BIF part, 'floating' hematite and greenalite particles (< 1 μm) are concentrated in microspheroids, or polygons. These are surrounded by inclusion-free chert (Fig. 6c-d), a texture that has been observed before by Rasmussen et al. (2017) in greenalite-rich but hematite–poor BIF and interpreted as preserved diagenetic shrinkage cracks. These were likely to have been formed during the conversion of silica into quartz during burial dehydration. Since both hematite and greenalite are enveloped in our samples by these shrinkage cracks, and neither of the minerals seems to have overgrown the other one, they both predate diagenetic silica dehydration and are likely to be primary phases.

However, these minerals cannot be formed under the same redox conditions. Greenalite nanoparticles are thought to be the primary precipitates from deep, ferruginous and mildly alkaline seawaters. They would be the first minerals to crystallise from amorphous Fe(II)-silicate gel deposits (Rasmussen et al., 2017). In contrast, the formation of Fe (III) oxyhydroxides (and subsequently hematite) requires more oxidising conditions. The co-existence of hematite and greenalite in our rocks can therefore only be explained if either time or space separated their formation.

A simple solution to this problem could be that the minerals precipitated from different parts of a redox gradient through the water column. The ferric oxyhydroxides would then stem from the shallowest, more oxidising part, whereas the ferrous silicates would have precipitated out of deeper, more reducing waters. It is also possible that temporal changes in the shape of this redox profile would have provoked precipitation from alternately ferric and ferrous particles. Once formed in the water column and precipitated on the seafloor, both phases could have resided in a meta-stable state.

Such a model matches with our observations, including the absence of greenalite in the Hotazel lutite part of the drill-core. Here, shallower

and more oxidising conditions would have allowed precipitation of Fe (III) oxyhydroxides only. In the Hotazel BIF part, representing a more distal setting, the influence of deep-marine, reducing waters would have been greater and enabled the precipitation of ferrous silicates.

It remains uncertain whether the hematite-free spheroidal chert structures rimmed by networks of nano-scale hematite are a primary or secondary feature (Fig. 6a). These textures were only found in jasper lenses or bulges of the Hotazel lutite. Contrary to in the Hotazel BIF part, no primary bedding has been preserved here (due to wave agitation or SSD), so inspection for layer truncation of the microspheroidal textures (which would argue for a secondary origin) is not possible. If they represent a preserved primary texture, they could reflect flocculation of colloidal silica via adsorption of Fe(III) oxyhydroxide particles: in silica-supersaturated waters, flocculation of silica is catalysed by the bridging effect of adsorbing ferric oxyhydroxide particles onto the surface of the colloidal silica (Williams and Crerar, 1985). Alternatively, these spheroidal structures could represent destroyed polygonal chert structures, developing in zones which have experienced higher degrees of recrystallisation (Rasmussen et al., 2017).

Primary, nano-sized hematite is in marked contrast to the larger (> 1 μm), rod-like hematite crystals showing radiating forms, which occur disseminated in the mudstones in close association with other Fe minerals (e.g. magnetite) or replacing stilpnomelane and/or chlorite fibres (Fig. 6e-f). These characteristics are clearly attributed to mineral replacement reactions by secondary hematite, possibly formed via infiltration of O_2-bearing fluids after lithification (e.g. Rasmussen et al., 2014, 2016). The microplaty hematite observed in the veins at the contact with the Ongeluk is analogous to secondary hematite ore (e.g. Morris, 2012). The spongy hematite aggregates that have intergrown or overgrown hematite-greenalite micropolygons (in the Hotazel BIF layers) were clearly formed at a later stage than nano-scale hematite (and greenalite). However, they could possibly have retained a primary seawater Fe signal and only have experienced crystal growth via dissolution-reprecipitation.

5.2.3. Seawater origin of hematite-chert

The PAAS-normalised REE + Y characteristics of the hematite-chert samples (Section 4.3.2) are very similar to those established from typical Archean/early Proterozoic IFs (e.g. Bau et al., 1997; Derry and Jacobsen, 1990; Bolhar et al., 2004; Planavsky et al., 2010). Based on the assumption that minimal fractionation occurs within the lanthanides during scavenging and co-precipitation with Fe from the water column, these IFs have commonly been inferred to directly have trapped the REE + Y signature of the ancient seawater (e.g. Derry and Jacobsen, Bau et al., 1996; Bolhar et al., 2004). Similarly, hematite Fe from this study is likely to have had a seawater origin.

The small to moderately positive Eu anomalies hint at a high-T hydrothermal fluid contribution, though this is a common feature for Precambrian IFs. The oceans at that time are thought to have been universally enriched in mantle-derived REE + Y compared to the modern ocean due to a global-scale enhanced supply of black smoker-type high-T hydrothermal activity (e.g. Derry and Jacobsen, 1990). Hence, the presence of a hydrothermal REE + Y source does not mean that all the Fe(II) originates from nearby, recently discharged hydrothermal fluids (e.g. related to the Ongeluk volcanism). Moreover, the strength of the measured Eu anomalies seems unrelated to the stratigraphic distance from the Ongeluk volcanics (Suppl. F6), and thus shows no indications for progressive dilution of a hydrothermal source with time (or distance). Only the $(Eu/Eu^*)_{SN}$ of the most proximate sample (sample 16) is significantly larger than that of the other samples, and might indicate some direct hydrothermal influence in the immediate vicinity of the Ongeluk volcanics (< 11 cm from the Ongeluk-Hotazel contact).

The clear difference in the level of LREE depletion between the REE + Y profiles of BIF and lutite jasper (Section 4.3.2) presumably reflects a change in seawater depth. In modern seawater, LREE depletion reflects competition in particle-solution interactions due to lanthanide contraction, in which the larger particles, i.e. the light REE are forming carbonate ion complexes to a lesser extent than the heavier REE. As a result, the LREE are more easily scavenged from the seawater by adsorption processes (e.g. Byrne and Kim, 1990; Quinn et al., 2004). However, the level of LREE depletion is generally much lower for shallow ocean-margin waters than for the deep open-ocean. This disparity most likely reflects the influence of continental drainage: rivers have rather flat, much less evolved (LREE depleted) REE + Y profiles due to their lower pH and shorter residence times (Elderfield et al., 1990). Consequently, the REE + Y budget of marginal seas represents that of a mix between more LREE-depleted, long-evolved seawater and less LREE-depleted riverine water. Accordingly, the dichotomy between the REE + Y profiles of BIF (i.e. deep-marine) and lutite (i.e. shallow-marine) jasper presumably demonstrates that they formed in more distal respectively proximal marine settings. Contamination of the lutite samples with detrital (lithogenic) material could alternatively explain the clear difference in $(Pr/Yb)_{SN}$ compared to the BIF samples, yet no correlation exists between the Zr content and the $(Pr/Yb)_{SN}$ (Suppl. F6).

The REE + Y distribution pattern of the hematite- and greenalite-bearing BIF layer bears much similarity with that of hematite-chert from Hamersley BIFs (Alibert, 2016). Despite its abundance, the contribution of greenalite apparently has little to no effect on the total REE + Y budget. Being the first study to present REE + Y of hematite only instead of bulk-rock BIF data, Alibert argues that hematite(-chert) REE + Y patterns are not directly seawater-like, but instead show features typical for K_d-dependent equilibration with pore-water during dissolution and reprecipitation from Si-Fe-OH precursors. This explains why the $(Pr/Yb)_{SN}$ values (ca 0.03) are lower than those of deep open-ocean water ($(Pr/Yb)_{SN}$ > 0.10). If hematite would have formed from ferrihydrite by solid-state diffusion it should have maintained its seawater-like REE + Y pattern. Hence, the rare-earth patterns support our previous interpretation for the origin of type II, nano-scale hematite grains, which would have lost part of their original seawater REE + Y, but have retained their primary seawater Fe signal.

5.3. Fe isotope interpretation

5.3.1. Fe isotopic imprint of hydrothermal alteration

Relatively large Fe isotopic variations occur (up to 1.1‰) in the Earth's mantle (Williams et al., 2005), yet the igneous rocks of the crust are generally very homogeneous, showing slightly positive δ^{56}Fe values with an average of ca 0.13‰ (e.g. Beard et al., 2003; Poitrasson et al., 2004; Schoenberg et al., 2009; Craddock et al., 2013; Teng et al., 2013). The remarkably low bulk rock δ^{56}Fe composition of the Ongeluk volcanics (OF1-3; ca −0.7‰) is therefore anomalous. However, studies have shown (Sharma et al., 2001; Rouxel et al., 2003) that significant Fe isotope fractionation can occur during seawater-basalt alteration (both low- and high-T) as a result of the extensive redox reactions, dissolution and precipitation of Fe-bearing minerals that take place. During hydrothermal circulation in suboxic mid-ocean ridge (MOR) settings, dissolution of the original igneous phases coincides with the preferential removal of ^{54}Fe over ^{56}Fe, resulting in Fe isotopically enriched basalts of up to +1–2‰ and isotopically light hydrothermal fluids ranging from −0.69‰ to −0.12‰ (Sharma et al., 2001; Beard et al., 2003; Severmann et al., 2004; Rouxel, 2008). The dissolved Fe(II) load of these fluids becomes more and more isotopically depleted during progressive alteration. ^{54}Fe is preferentially dissolved during dissolution of the primary minerals (kinetic effect) and, during mixing with oxidising seawater, ^{56}Fe is also preferentially removed from the fluids during the precipitation of isotopically heavier, secondary minerals such as Fe(III) oxyhydroxides and Fe(III)-rich clays (Polyakov and Mineev, 2000). According to the Rayleigh fractionation model of Rouxel et al. (2003), the first ferric precipitates would have positive δ^{56}Fe values at the start of the precipitation, but with ongoing alteration and oxidation would become gradually more negative and could

eventually produce $\delta^{56}Fe$ values down to −3.0‰ after deposition of 90% of the original dissolved Fe(II) pool. Hence, the very depleted Fe isotopic composition of the Ongeluk volcanics records alteration by isotopically depleted hydrothermal fluids (with $\delta^{56}Fe < -0.7$‰), and moreover, provides strong evidence for the oxidation potential of the shallow parts of the Transvaal basin, which enhanced the isotopic depletion.

5.3.2. Fe isotope signature of the water column

The $\delta^{56}Fe$ value of primary hematite reflects 1) the $\delta^{56}Fe$ value of the water column at the time of deposition and 2) the combined isotopic fractionation effect during the redox change from $Fe(II)_{aq} \rightarrow Fe(III)$ and $Fe(III) \rightarrow Fe(OH)_3$ (assuming no fractionation occurred during further hematite formation):$\Delta^{56}Fe_{Fe(II)aq–hematite} = \delta^{56}Fe_{Fe(II)aq} - \delta^{56}Fe_{hematite}$,which is ca −1.0‰ for both microbially mediated and abiotic Fe(II) oxidation (Bullen et al., 2001; Beard and Johnson, 2004; Croal et al., 2004; Balci et al., 2006; Beard et al., 2010). The $\delta^{56}Fe$ values measured in the hematite-rich samples presented in this study are all below −0.26‰, which thus represents a maximum $\delta^{56}Fe$ value for the dissolved Fe(II) pool at the time of deposition. Assuming partial oxidation and equilibrium fractionation to have occurred, this indicates > 1‰, possibly nearing 2‰ depletion with respect to estimated Archean seawater ($\delta^{56}Fe = 0$‰). Because the $\delta^{56}Fe$ values were measured in largely primary hematite, they cannot be the result of microbial Fe(III) reduction (which is similarly capable of producing very depleted $\delta^{56}Fe$ values in the sediment (e.g. Johnson et al., 2008)), and hence testify for an isotopically very light water column.

Fe silicates, carbonates and oxides have different redox states and bonding types and therefore different fractionation factors with respect to Fe (Schauble, 2004; Anbar and Rouxel, 2007). The noticeably lower $\delta^{56}Fe$ of Ca- and Mg-, Al-rich content of respectively samples HF6 (−0.93‰) and HF5 (−1.07‰), compared to the stratigraphically adjacent samples HF7 (−0.50‰) and HF4 (−0.49‰), is therefore likely related to Fe mineral impurities, rather than recording inherent changes in the $\delta^{56}Fe$ composition of the water column with time. The fractionation effect between dissolved Fe(II) and $FeCO_3$ is much larger than between Fe(II) and $Fe(OH)_3$, as experimentally determined $\Delta^{56}Fe_{Fe(II)aq–FeCO3}$ values range from 0.0‰ up to +1.0‰ (e.g. Wiesli et al., 2004; Johnson et al., 2005). Therefore, Fe carbonates generally yield considerably lower $\delta^{56}Fe$ values (1–4‰ lighter) than ferric oxyhydroxides (Bullen et al., 2001; Beard and Johnson, 2004; Beard et al., 2010; Johnson et al., 2008). The elevated Fe carbonate content of sample HF6 therefore most likely explains its lower $\delta^{56}Fe$ compared to the hematite-dominated HF7. The very high Al content of HF5 indicates a substantial contribution of stilpnomelane and/or chlorite. We do not know the precise isotopic composition of Ongeluk-derived chlorite, but the average bulk-rock $\delta^{56}Fe$ value of the chlorite-dominated Ongeluk volcanics (–0.7‰), suggests it was low as well. Stilpnomelane may both have grown from precursor chlorite and hydrogenous Fe silicate gels (Konhauser et al., 2002, 2007; Rasmussen et al., 2015). In any case, during diagenetic and metamorphic growth stilpnomelane would have preferentially incorporated ^{54}Fe in its crystal lattice, since Fe(II)-bearing minerals are predicted to obtain light Fe in equilibrium as compared to Fe(III) fluids and minerals (Polyakov and Mineev, 2000). Hence, we suspect that the Fe silicates have shifted the $\delta^{56}Fe$ composition of HF5 also towards “lower” values. In other words, it more closely matches the $\delta^{56}Fe$ of the original seawater Fe(II). The same would apply to the $\delta^{56}Fe$ of HF1, which contains a substantial portion of primary greenalite nanoparticles. Regarding the moderately elevated Mg, Al and Ca content of HF3-4, mineral impurities might similarly have had a negative effect on their $\delta^{56}Fe$ value, though to a relatively minor extent.

The net increase in $\delta^{56}Fe$ from HF7 to HF1 – corresponding to the shift from a lutitic lithology towards a BIF – is small (+0.24‰), but reaches beyond the external reproducibility limits (± 0.10‰ 2 S.D.) and is systematic with stratigraphic height. Moreover, taking into account the mineral-specific fractionation effects, this difference might have been greater for the water column due to the presence of greenalite in HF1. We interpret this shift as an indication of an isotopic gradient for dissolved Fe(II) in the primary water column, in which the deeper waters were less oxidising and therefore slightly less depleted in ^{56}Fe than the shallowest parts. In part, this shift might further correspond to the progressive dilution of Ongeluk hydrothermal Fe(II) fluids, which are more strongly depleted in $\delta^{56}Fe$ than the ambient seawater.

5.4. Redox evolution of the Transvaal basin

The negative $\delta^{56}Fe$ values of primary hematite-rich chert ($\delta^{56}Fe = -0.50$‰) and mixed primary hematite- and greenalite-rich chert ($\delta^{56}Fe = -0.26$) at the base of the Hotazel clearly reflect the effect of a Rayleigh distillation process. Due to the continuous production of photosynthetic O_2 in the shallow parts of the ocean, dissolved Fe(II) must have been continuously oxidised, thereby causing the progressive depletion of the seawater $\delta^{56}Fe$ signal. However, the Fe isotopic signature ($\delta^{56}Fe$ between −1.6 and −2.4‰) of the transitional hematite-lutite intervals at the contacts between the BIF and manganese ore higher up in the stratigraphy of the Hotazel Formation (Tsikos et al., 2010) is 1–2‰ more depleted. These intervals are furthermore, apart from hematite-, much more Mn(II)-rich. Bulk-rock Mn concentrations typically range between 5 and 25 wt%, hosted predominantly in kutnahorite, Mn-calcite and to a minor extent in Fe Mn-dolomite (Tsikos et al., 2010). Based on their sedimentary structures, we consider these intervals to be facies-equivalent to the Hotazel lutite interval from this study, situated immediately above the Ongeluk. Our rocks, however, are poorer in Mn(II); Mn is only hosted in the crystal lattices of authigenic calcite and dolomite (we consider Mn-ilmenite to be of detrital origin). Kutnahorite is the dominant Mn-bearing carbonate in the transitional lutites higher up, containing more than 20 wt% of Mn (Mhlanga et al., 2015), but it is absent in our rocks. Moreover, XRF data indicate bulk-rock Mn concentrations of < 1 wt%. This means that the Fe/Mn levels of the upper water column at the onset of Hotazel deposition (at the base of the Hotazel Formation) were higher compared to later in time (as expressed several metres higher up in the Hotazel stratigraphy).

Oxidation of Mn(II) requires higher redox potentials than oxidation of Fe(II). In addition, oxidised Mn as Mn(III) and Mn(IV) is a highly effective oxidiser of Fe(II), which results in effective recycling of Mn(II) back into the water column (Canfield et al., 2005). Some of this Mn(II) may be taken up by co-precipitating carbonates (Mhlanga et al., 2015). The low Mn content and predominance of primary hematite at the base of the Hotazel Formation therefore indicate that redox processes were still dominated by oxidation of aqueous Fe(II), and hence that the oxidation potential of the seawater was still limited. Further evidence is provided by the absence of a true negative Ce anomaly in all hematite REE + Y distribution patterns (Suppl. F5). In aerobic waters, negative Ce anomalies arise from the oxidation of Ce^{3+} to less soluble Ce^{4+} and subsequent removal from the water column by scavenging on settling particles, predominantly Mn oxyhydroxide particles (Sholkovitz et al., 1994). The lack of a true negative Ce anomaly in hematite-chert at the base of the Hotazel therefore indicates that oxygen levels of the water column were still too low to oxidise Ce(III). This contrasts with previous claims about the existence of a negative Ce anomaly in the Hotazel Formation (Kirschvink et al., 2000; Kopp et al., 2005; Kirschvink and Kopp, 2008; Gumsley et al., 2017).

We propose that a combination of two phenomena could explain the up to 2‰ difference between the $\delta^{56}Fe$ values of hematite-rich chert at the base of the Hotazel and the hematite-rich bulk-rock samples from the transitional hematite-lutites higher up in the sequence. Firstly, the ferric oxyhydroxides precipitated against a different part of an Fe isotopic gradient across the water column: the oxyhydroxides at the base of the Hotazel Formation originated from isotopically heavier waters than the ferric precipitates from the transitional hematite-lutites that

border the sedimentary Mn ore layers higher up. Secondly, the hematite from this study is the product of partial oxidation of a dissolved Fe(II) reservoir and so isotopic fractionation ($\Delta^{56}Fe_{Fe(II)aq-hematite} = -1‰$) produced heavier $\delta^{56}Fe$ values for the ferric precipitate. In contrast, the transitional lutites essentially reflect semi-quantitative oxidation of the dissolved Fe(II) pool, and so the precipitate obtained a $\delta^{56}Fe$ close to that of its source fluid (Beard et al., 2003; Rouxel et al., 2003; Anbar et al., 2005; Markl et al., 2006). The latter would have resulted from the ongoing oxidation of Fe(II) with photosynthetic O_2, gradually thinning out the Fe(II) inventory in the shallowest parts of the ocean, and eventually leaving behind a very limited pool of isotopically very light Fe(II). At the same time, proceeding aerobic conditions and hence removal of dissolved Fe(II) would gradually enrich the seawater's Mn-Fe ratio over time and eventually give rise to precipitation of Mn-rich deposits. Water column overturning processes such as upwelling and storm events would have replenished the uppermost layers with new, less depleted Fe(II), and so deposition of strongly depleted hematite-lutites and sedimentary Mn ores could have been replicated through time.

5.5. Implications for the timing of the GOE

The isotopic and geochemical characteristics at the initial stages of the Hotazel IF environment apparently were not as intense as reported upward in the stratigraphic record. Yet, the stratigraphically underlying BIFs of the Ghaap Group are characterised by the predominance of ferrous or mixed-valence Fe minerals (magnetite, greenalite), very low Mn concentrations and near-zero to positive $\delta^{56}Fe$ values (Beukes and Klein, 1990; Johnson et al., 2003; Beukes and Gutzmer, 2008; Rasmussen et al., 2017). The isotopically depleted, primary hematite-rich yet Mn-poor strata at the basal 2.8 m of the Hotazel Formation therefore seem to be a transitional interval between typical ferruginous BIF deposition and Mn-oxide deposition in more oxygenated surface waters. Our data thus broadly fit with a Rayleigh fractionation model, in which the Transvaal basin underwent isotopic and chemical evolution as a consequence of continuous photosynthetic oxygen production. During deposition of the Mn-rich strata of the Hotazel, the surface ocean's reducing power would have become sufficiently weak to allow for the accumulation of free O_2 in the atmosphere, possibly contributing to the onset of the GOE. In this view, the Mn-rich strata in the main overlying part of the ca 2.4 Ga HotazelFormation might be syn-GOE, embodying one of the terminal marine O_2 sinks of that time and providing a strong cause for the disappearance of MIF-S around 2.33 Ga (Luo et al., 2016). In contrast, our results from the base of the Hotazel imply that significant oxygenation had not yet commenced at the onset of the Hotazel deposition, and should thus be considered pre-GOE.

. This interpretation contrasts with previous models which placed the GOE before the Hotazel, in the immediate aftermath of the Makganyene glaciation at 2.426 Ga (Kirschvink et al., 2000; Kopp et al., 2005; Kirschvink and Kopp, 2008; Gumsley et al., 2017). Ice cap retreat would have triggered extensive Mn(IV) deposition in an oxygenated, post-GOE marine environment. They fortify their model by mentioning the presence of a negative Ce anomaly. However, our rocks do not contain either Mn-oxides or negative Ce anomalies. To explain the lack of negative Ce anomalies in the stratigraphically overlying Mooidraai carbonates (Bau and Alexander, 2006; Kunzmann et al., 2014), and even more critically the presence of MIF-S in the lower Duitschland Formation (Guo et al., 2009), they refer to the dynamic state of the GOE, i.e. the rise of atmospheric O_2 was characterised by oscillations. After the initial oxygenation at the Makganyene event, the atmosphere must have temporally returned to anoxic conditions. In contrast, our results are in favour of a much simpler model (i.e. Rayleigh distillation), which does not demand such dramatic O_2 fluctuations to have occurred and which does not need to move the GOE before the Hotazel Formation. However, we do not intend to question here that the Makganyene glacial event could be mechanistically linked to the rise of atmospheric oxygen. Leaching of small amounts of photosynthetic O_2 prior to the GOE could have reacted with methane, significantly reducing the atmosphere's greenhouse effect and hence triggering glaciation.

6. Conclusion

Our observations show that the Ongeluk volcanics experienced significant hydrothermal alteration upon extrusion into the shallow Transvaal basin. The Ongeluk's remarkably low bulk-rock $\delta^{56}Fe$ signature and the presence of seawater percolation paths indicate interaction with seawater that contained some dissolved O_2.

However, the Ongeluk hydrothermal fluids had a negligible effect on the conformably overlying hematite-rich lutitic sediments of the Hotazel Formation. Sedimentation in the shallow water column was controlled by precipitation of Fe(III) oxyhydroxides from seawater. In the deeper parts, ferrous silicates could settle from more reducing waters.

Negative $\delta^{56}Fe$ Fe isotope values measured in primary hematite-rich chert mark the first, unambiguous point in the stratigraphy of the Transvaal Supergroup where the Fe isotopic signature becomes permanently depleted, representing partial precipitation from an isotopically very light Fe(II) pool. However, the $\delta^{56}Fe$ composition of the hematite-lutites at the transitions between BIF and Mn ore higher up in the stratigraphy of the Hotazel Formation is 1–2‰ lower. This can be explained by quantitative oxidation of an isotopically lighter as well as much more limited Fe(II) pool. Moreover, low bulk-rock Mn concentrations and the lack of a true negative Ce anomaly suggest O_2 concentrations at the initial stages of the Hotazel IF depositional environment were still limited.

The basal 2.8 ms of the Hotazel form a transitional interval when compared between ferruginous seawater ($\delta^{56}Fe = 0$) conditions recorded in the lower BIF portion of the basin (Ghaap Group) and redox-evolved surface water ($\delta^{56}Fe \ll 0$) in which Mn oxides could form. Our results are thus compatible with a Rayleigh effect related to a build-up of photosynthetic O_2 concentrations in the upper parts of the basin. The absence of a strongly reducing Fe(II) pool would have allowed accumulation of free O_2 in the atmosphere, contributing to the disappearance of MIF-S later in time and higher up in the stratigraphy. In this view, deposition of the Mn-rich layers higher up in the Hotazel Formation may have been right at the onset of atmospheric oxygenation, whereas that of the lowermost part of the Hotazel would have preceded the GOE. Our findings thus question previous models which placed the Hotazel Formation in the aftermath of the GOE.

Acknowledgements

This study was supported by grant 2.2.3c from the Netherlands Research Centre for Integrated Solid Earth Science. We are grateful to Helen de Waard, Ton Zalm, Tilly Bouten, Otto Stiekema, Leonard Bik, Peter van Krieken en Anita van Leeuwen-Tolboom of the Earth Sciences Department, Utrecht University, The Netherlands, for their assistance in most of the analytical procedures. We further acknowledge F. von Blanckenburg from the German Research Centre for Geosciences, Potsdam, for giving us the opportunity to use the MC-ICP-MS, and the technical staff for their assistance with the Fe isotope measurements.

Appendix A. Supplementary data

Supplementary data associated with this article can be found, in the online version, at http://dx.doi.org/10.1016/j.precamres.2017.12.025.

References

Ahn, J.H., Buseck, P.R., 1990. Hematite nanospheres of possible colloidal origin from a Precambrian banded iron formation. Science 250 (4977), 111–113.
Alibert, C., 2016. Rare earth elements in Hamersley BIF minerals. Geochim. Cosmochim.

Acta 184, 311–328.
Anbar, A.D., Roe, J.E., Barling, J., Nealson, K.H., 2000. Nonbiological fractionation of iron isotopes. Science 288 (5463), 126–128.
Anbar, A.D., Jarzecki, A.A., Spiro, T.G., 2005. Theoretical investigation of iron isotope fractionation between Fe $(H_2O)_6^{3+}$ and Fe $(H_2O)_6^{2+}$: implications for iron stable isotope geochemistry. Geochim. Cosmochim. Acta 69 (4), 825–837.
Anbar, A.D., Rouxel, O., 2007. Metal stable isotopes in paleoceanography. Annu. Rev. Earth Planet. Sci. 35, 717–746.
Anbar, A.D., Duan, Y., Lyons, T.W., Arnold, G.L., Kendall, B., Creaser, R.A., Ellipsis & Buick, R., 2007. A whiff of oxygen before the great oxidation event? Science 317 (5846), 1903–1906.
Ayres, D.E., 1972. Genesis of iron-bearing minerals in banded iron formation mesobands in the Dales Gorge Member, Hamersley Group, Western Australia. Econ. Geol. 67 (8), 1214–1233.
Balci, N., Bullen, T.D., Witte-Lien, K., Shanks, W.C., Motelica, M., Mandernack, K.W., 2006. Iron isotope fractionation during microbially stimulated Fe (II) oxidation and Fe (III) precipitation. Geochim. Cosmochim. Acta 70 (3), 622–639.
Bao, S.X., Zhou, H.Y., Peng, X.T., Ji, F.W., Yao, H.Q., 2008. Geochemistry of REE and yttrium in hydrothermal fluids from the Endeavour segment, Juan de Fuca Ridge. Geochem. J. 42 (4), 359–370.
Bau, M., Dulski, P., 1996. Distribution of yttrium and rare-earth elements in the Penge and Kuruman iron-formations, Transvaal Supergroup, South Africa. Precambr. Res. 79 (1), 37–55.
Bau, M., Koschinsky, A., Dulski, P., Hein, J.R., 1996. Comparison of the partitioning behaviours of yttrium, rare earth elements, and titanium between hydrogenetic marine ferromanganese crusts and seawater. Geochim. Cosmochim. Acta 60 (10), 1709–1725.
Bau, M., Höhndorf, A., Dulski, P., Beukes, N.J., 1997. Sources of rare-earth elements and iron in Paleoproterozoic iron-formations from the Transvaal Supergroup, South Africa: evidence from neodymium isotopes. J. Geol. 121–129.
Bau, M., Romer, R.L., Lüders, V., Beukes, N.J., 1999. Pb, O, and C isotopes in silicified Mooidraai dolomite (Transvaal Supergroup, South Africa): implications for the composition of Paleoproterozoic seawater and 'dating'the increase of oxygen in the Precambrian atmosphere. Earth Planet. Sci. Lett. 174 (1), 43–57.
Bau, M., Alexander, B., 2006. Preservation of primary REE patterns without Ce anomaly during dolomitization of Mid-Paleoproterozoic limestone and the potential re-establishment of marine anoxia immediately after the "Great Oxidation Event". S. Afr. J. Geol. 109 (1–2), 81–86.
Bau, M., Schmidt, K., Koschinsky, A., Hein, J., Kuhn, T., Usui, A., 2014. Discriminating between different genetic types of marine ferro-manganese crusts and nodules based on rare earth elements and yttrium. Chem. Geol. 381, 1–9.
Beard, B.L., Johnson, C.M., Cox, L., Sun, H., Nealson, K.H., Aguilar, C., 1999. Iron isotope biosignatures. Science 285 (5435), 1889–1892.
Beard, B.L., Johnson, C.M., Skulan, J.L., Nealson, K.H., Cox, L., Sun, H., 2003. Application of Fe isotopes to tracing the geochemical and biological cycling of Fe. Chem. Geol. 195 (1), 87–117.
Beard, B.L., Johnson, C.M., 2004. Fe isotope variations in the modern and ancient earth and other planetary bodies. Rev. Mineral. Geochem. 55 (1), 319–357.
Beard, B.L., Handler, R.M., Scherer, M.M., Wu, L., Czaja, A.D., Heimann, A., Johnson, C.M., 2010. Iron isotope fractionation between aqueous ferrous iron and goethite. Earth Planet. Sci. Lett. 295 (1), 241–250.
Bekker, A., Holland, H.D., Wang, P.L., Rumble, D.I.I.I., Stein, H.J., Hannah, J.L., Ellipsis & Beukes, N.J., 2004. Dating the rise of atmospheric oxygen. Nature 427 (6970), 117–120.
Bekker, A., Slack, J.F., Planavsky, N., Krapež, B., Hofmann, A., Konhauser, K.O., Rouxel, O.J., 2010. Iron formation: the sedimentary product of a complex interplay among mantle, tectonic, oceanic, and biospheric processes. Econ. Geol. 105 (3), 467–508.
Beukes, N.J., 1983. Palaeoenvironmental setting of iron-formations in the depositional basin of the Transvaal Supergroup, South Africa. Dev. Precambr. Geol. 6, 131–198.
Beukes, N.J., Klein, C., 1990. Geochemistry and sedimentology of a facies transition—-from microbanded to granular iron-formation—in the early Proterozoic Transvaal Supergroup, South Africa. Precambr. Res. 47 (1–2), 99–139.
Beukes, N.J., Gutzmer, J.E.N.S., 2008. Origin and paleoenvironmental significance of major iron formations at the Archean-Paleoproterozoic boundary. Rev. Econ. Geol. 15, 5–47.
Bolhar, R., Kamber, B.S., Moorbath, S., Fedo, C.M., Whitehouse, M.J., 2004. Characterisation of early Archaean chemical sediments by trace element signatures. Earth Planet. Sci. Lett. 222 (1), 43–60.
Brasier, M., McLoughlin, N., Green, O., Wacey, D., 2006. A fresh look at the fossil evidence for early Archaean cellular life. Philos. Trans. R Soc. Lond. B Biol. Sci. 361 (1470), 887–902.
Buick, R., 2008. When did oxygenic photosynthesis evolve? Philos. Trans. R Soc. Lond. B Biol. Sci. 363 (1504), 2731–2743.
Bullen, T.D., White, A.F., Childs, C.W., Vivit, D.V., Schulz, M.S., 2001. Demonstration of significant abiotic iron isotope fractionation in nature. Geology 29 (8), 699–702.
Button, A., 1976. Transvaal and Hamersley Basins: Review of basin development and mineral deposits (No. 107). University of the Witwatersrand, Economic Geology Research Unit.
Byrne, R.H., Kim, K.H., 1990. Rare earth element scavenging in seawater. Geochim. Cosmochim. Acta 54 (10), 2645–2656.
Campbell, I.H., Allen, C.M., 2008. Formation of supercontinents linked to increases in atmospheric oxygen. Nat. Geosci. 1 (8), 554–558.
Canfield, D.E., 1998. A new model for Proterozoic ocean chemistry. Nature 396 (6710), 450–453.
Canfield, D.E., Thamdrup, B., Kristensen, E., 2005. Aquatic Geomicrobiology. Advances in Marine Biology. vol. 48. Elsevier, San Diego, pp. 640.
Cheney, E.S., 1996. Sequence stratigraphy and plate tectonic significance of the Transvaal succession of southern Africa and its equivalent in Western Australia. Precambr. Res. 79 (1), 3–24.
Claire, M.W., Catling, D.C., Zahnle, K.J., 2006. Biogeochemical modelling of the rise in atmospheric oxygen. Geobiology 4 (4), 239–269.
Cornell, D.H., Schütte, S.S., 1995. A volcanic-exhalative origin for the world's largest (Kalahari) manganese field. Miner. Deposita 30 (2), 146–151.
Cornell, D.H., Schütte, S.S., Eglington, B.L., 1996. The Ongeluk basaltic andesite formation in Griqualand West, South Africa: submarine alteration in a 2222 Ma Proterozoic sea. Precambr. Res. 79 (1), 101–123.
Craddock, P.R., Warren, J.M., Dauphas, N., 2013. Abyssal peridotites reveal the near-chondritic Fe isotopic composition of the Earth. Earth Planet. Sci. Lett. 365, 63–76.
Croal, L.R., Johnson, C.M., Beard, B.L., Newman, D.K., 2004. Iron isotope fractionation by Fe (II)-oxidizing photoautotrophic bacteria. Geochim. Cosmochim. Acta 68 (6), 1227–1242.
Czaja, A.D., Johnson, C.M., Roden, E.E., Beard, B.L., Voegelin, A.R., Nägler, T.F., Ellipsis & Wille, M., 2012. Evidence for free oxygen in the Neoarchean ocean based on coupled iron–molybdenum isotope fractionation. Geochim. Cosmochim. Acta 86, 118–137.
Czaja, A.D., Johnson, C.M., Beard, B.L., Roden, E.E., Li, W., Moorbath, S., 2013. Biological Fe oxidation controlled deposition of banded iron formation in the ca. 3770Ma Isua Supracrustal Belt (West Greenland). Earth Planet. Sci. Lett. 363, 192–203.
de Kock, M.O., Evans, D.A., Beukes, N.J., 2009. Validating the existence of Vaalbara in the Neoarchean. Precambr. Res. 174 (1), 145–154.
Derry, L.A., Jacobsen, S.B., 1990. The chemical evolution of Precambrian seawater: evidence from REEs in banded iron formations. Geochim. Cosmochim. Acta 54 (11), 2965–2977.
Eigenbrode, J.L., Freeman, K.H., 2006. Late Archean rise of aerobic microbial ecosystems. Proc. Natl. Acad. Sci. 103 (43), 15759–15764.
Eigenbrode, J.L., Freeman, K.H., Summons, R.E., 2008. Methylhopane biomarker hydrocarbons in Hamersley Province sediments provide evidence for Neoarchean aerobiosis. Earth Planet. Sci. Lett. 273 (3), 323–331.
Elderfield, H., Upstill-Goddard, R., Sholkovitz, E.R., 1990. The rare earth elements in rivers, estuaries, and coastal seas and their significance to the composition of ocean waters. Geochim. Cosmochim. Acta 54 (4), 971–991.
Farquhar, J., Bao, H., Thiemens, M., 2000. Atmospheric influence of Earth's earliest sulfur cycle. Science 289 (5480), 756–758.
Gaillard, F., Scaillet, B., Arndt, N.T., 2011. Atmospheric oxygenation caused by a change in volcanic degassing pressure. Nature 478 (7368), 229–232.
German, C.R., Higgs, N.C., Thomson, J., Mills, R., Elderfield, H., Blusztajn, J., Ellipsis & Bacon, M.P., 1993. A geochemical study of metalliferous sediment from the TAG Hydrothermal Mound, 26° 08′ N, Mid-Atlantic Ridge. J. Geophys. Res. Solid Earth 98 (B6), 9683–9692.
Grobler, N.J., Botha, B.J.V., 1976. Pillow-lavas and hyaloclastite in the Ongeluk Andesite Formation in a road-cutting west of Griquatown, South Africa. Trans. Geol. Soc. S. AFT. 79, 53–57.
Gumsley, A.P., Chamberlain, K.R., Bleeker, W., Söderlund, U., de Kock, M.O., Larsson, E. R., Bekker, A., 2017. Timing and tempo of the Great Oxidation Event. In: Proceedings of the National Academy of Sciences, 201608824.
Guo, Q., Strauss, H., Kaufman, A.J., Schröder, S., Gutzmer, J., Wing, B., Ellipsis & Farquhar, J., 2009. Reconstructing Earth's surface oxidation across the Archean-Proterozoic transition. Geology 37 (5), 399–402.
Gutzmer, J., Beukes, N.J., 1996. Mineral paragenesis of the Kalahari manganese field, South Africa. Ore Geol. Rev. 11 (6), 405–428.
Han, T.M., 1978. Microstructures of magnetite as guides to its origin in some Precambrian iron-formations. Fortschr. Mineral. 56 (1), 105–142.
Haugaard, R., Pecoits, E., Lalonde, S., Rouxel, O., Konhauser, K., 2016. The Joffre banded iron formation, Hamersley Group, Western Australia: Assessing the palaeoenvironment through detailed petrology and chemostratigraphy. Precambr. Res. 273, 12–37.
Haymon, R.M., Kastner, M., 1981. Hot spring deposits on the East Pacific Rise at 21 N: preliminary description of mineralogy and genesis. Earth Planet. Sci. Lett. 53 (3), 363–381.
Hoashi, M., Bevacqua, D.C., Otake, T., Watanabe, Y., Hickman, A.H., Utsunomiya, S., Ohmoto, H., 2009. Primary haematite formation in an oxygenated sea 3.46 billion years ago. Nat. Geosci. 2 (4), 301–306.
Holland, H.D., 1984. The Chemical Evolution of the Atmosphere and Oceans. Princeton University Press.
Holland, H.D., 1999. When did the Earth's atmosphere become oxic? A reply. *Geochem. News* 100, 20–22.
Holland, H.D., 2006. The oxygenation of the atmosphere and oceans. Philos. Trans. R Soc. Lond. B Biol. Sci. 361 (1470), 903–915.
James, H.L., 1954. Sedimentary facies of iron-formation. Econ. Geol. 49 (3), 235–293.
Johnson, C.M., Skulan, J.L., Beard, B.L., Sun, H., Nealson, K.H., Braterman, P.S., 2002. Isotopic fractionation between Fe (III) and Fe (II) in aqueous solutions. Earth Planet. Sci. Lett. 195 (1), 141–153.
Johnson, C.M., Beard, B.L., Beukes, N.J., Klein, C., O'Leary, J.M., 2003. Ancient geochemical cycling in the Earth as inferred from Fe isotope studies of banded iron formations from the Transvaal Craton. Contrib. Miner. Petrol. 144 (5), 523–547.
Johnson, C.M., Roden, E.E., Welch, S.A., Beard, B.L., 2005. Experimental constraints on Fe isotope fractionation during magnetite and Fe carbonate formation coupled to dissimilatory hydrous ferric oxide reduction. Geochim. Cosmochim. Acta 69 (4), 963–993.
Johnson, C.M., Beard, B.L., Klein, C., Beukes, N.J., Roden, E.E., 2008. Iron isotopes constrain biologic and abiologic processes in banded iron formation genesis. Geochim. Cosmochim. Acta 72 (1), 151–169.
Kappler, A., Pasquero, C., Konhauser, K.O., Newman, D.K., 2005. Deposition of banded

iron formations by anoxygenic phototrophic Fe (II)-oxidizing bacteria. Geology 33 (11), 865–868.
Kirschvink, J.L., Gaidos, E.J., Bertani, L.E., Beukes, N.J., Gutzmer, J., Maepa, L.N., Steinberger, R.E., 2000. Paleoproterozoic snowball Earth: extreme climatic and geochemical global change and its biological consequences. Proc. Natl. Acad. Sci. 97 (4), 1400–1405.
Kirschvink, J.L., Kopp, R.E., 2008. Palaeoproterozoic ice houses and the evolution of oxygen-mediating enzymes: the case for a late origin of photosystem II. Philos. Trans. R Soc. Lond. B Biol. Sci. 363 (1504), 2755–2765.
Klein, C., 2005. Some Precambrian banded iron-formations (BIFs) from around the world: Their age, geologic setting, mineralogy, metamorphism, geochemistry, and origins. Am. Mineral. 90 (10), 1473–1499.
Klein, C., Beukes, N.J., 1989. Geochemistry and sedimentology of a facies transition from limestone to iron-formation deposition in the early Proterozoic Transvaal Supergroup, South Africa. Econ. Geol. 84 (7), 1733–1774.
Klein, C., Beukes, N.J., 1992. Proterozoic iron-formations. Dev. Precamb. Geol. 10, 383–418.
Konhauser, K.O., Hamade, T., Raiswell, R., Morris, R.C., Ferris, F.G., Southam, G., Canfield, D.E., 2002. Could bacteria have formed the Precambrian banded iron formations? Geology 30 (12), 1079–1082.
Konhauser, K.O., Amskold, L., Lalonde, S.V., Posth, N.R., Kappler, A., Anbar, A., 2007. Decoupling photochemical Fe (II) oxidation from shallow-water BIF deposition. Earth Planet. Sci. Lett. 258 (1), 87–100.
Konhauser, K.O., Planavsky, N.J., Hardisty, D.S., Robbins, L.J., Warchola, T.J., Haugaard, R., Ellipsis & Lyons, T.W., 2017. Iron formations: A global record of Neoarchaean to Palaeoproterozoic environmental history. Earth Sci. Rev. 172, 140–177.
Kopp, R.E., Kirschvink, J.L., Hilburn, I.A., Nash, C.Z., 2005. The Paleoproterozoic snowball Earth: a climate disaster triggered by the evolution of oxygenic photosynthesis. PNAS 102 (32), 11131–11136.
Krapež, B., Barley, M.E., Pickard, A.L., 2003. Hydrothermal and resedimented origins of the precursor sediments to banded iron formation: sedimentological evidence from the Early Palaeoproterozoic Brockman Supersequence of Western Australia. Sedimentology 50 (5), 979–1011.
Kump, L.R., Barley, M.E., 2007. Increased subaerial volcanism and the rise of atmospheric oxygen 2.5 billion years ago. Nature 448 (7157), 1033–1036.
Kunzmann, M., Gutzmer, J., Beukes, N.J., Halverson, G.P., 2014. Depositional environment and lithostratigraphy of the Paleoproterozoic Mooidraai Formation, Kalahari Manganese Field, South Africa. S. Afr. J. Geol. 117 (2), 173–192.
Kurzweil, F., Wille, M., Gantert, N., Beukes, N.J., Schoenberg, R., 2016. Manganese oxide shuttling in pre-GOE oceans–evidence from molybdenum and iron isotopes. Earth Planet. Sci. Lett. 452, 69–78.
Li, W., Czaja, A.D., Van Kranendonk, M.J., Beard, B.L., Roden, E.E., Johnson, C.M., 2013. An anoxic, Fe (II)-rich, U-poor ocean 3.46 billion years ago. Geochim. Cosmochim. Acta 120, 65–79.
Laznicka, P., 1992. Manganese deposits in the global lithogenetic system: Quantitative approach. Ore Geol. Rev. 7 (4), 279–356.
Luo, G., Ono, S., Beukes, N.J., Wang, D.T., Xie, S., Summons, R.E., 2016. Rapid oxygenation of Earth's atmosphere 2.33 billion years ago. Sci. Adv. 2 (5), e1600134.
Lyons, T.W., Reinhard, C.T., Planavsky, N.J., 2014. The rise of oxygen in Earth/'s early ocean and atmosphere. Nature 506 (7488), 307–315.
Markl, G., Von Blanckenburg, F., Wagner, T., 2006. Iron isotope fractionation during hydrothermal ore deposition and alteration. Geochim. Cosmochim. Acta 70 (12), 3011–3030.
Meng, D., Wu, X., Fan, X., Meng, X., Zheng, J., Mason, R., 2009. Submicron-sized fluid inclusions and distribution of hydrous components in jadeite, quartz and symplectite-forming minerals from UHP jadeite–quartzite in the Dabie Mountains, China: TEM and FTIR investigation. Appl. Geochem. 24 (4), 517–526.
Mhlanga, X. R., Tsikos, H., Boyce, A., Lyons, T.W., 2015. Primary iron-and manganese-carbonate deposition in the palaeoproterozoic hotazel formation, South Africa, and implications for the great oxidation event. In: AGU Fall Meeting Abstracts.
Miyano, T., Beukes, N.J., 1984. Phase relations of stilpnomelane, ferri-annite, and riebeckite in very low-grade metamorphosed iron-formations. S. Afr. J. Geol. 87 (2), 111–124.
Moore, J.M., Polteau, S., Armstrong, R.A., Corfu, F., Tsikos, H., 2012. The age and correlation of the Postmasburg Group, southern Africa: constraints from detrital zircon grains. J. Afr. Earth Sc. 64, 9–19.
Morris, R.C., 1993. Genetic modelling for banded iron-formation of the Hamersley Group, Pilbara Craton, Western Australia. Precambr. Res. 60 (1), 243–286.
Morris, R.C., 2012. Microplaty hematite—its varied nature and genesis. Aust. J. Earth Sci. 59 (3), 411–434.
Nel, C.J., Beukes, N.J., De Villiers, J.P.R., 1986. The Mamatwan manganese mine of the Kalahari manganese field. Mineral Deposits of Southern Africa. vol. 1. pp. 963–978.
Olson, S.L., Kump, L.R., Kasting, J.F., 2013. Quantifying the areal extent and dissolved oxygen concentrations of Archean oxygen oases. Chem. Geol. 362, 35–43.
Page, A.L., 1982. Methods of Soil Analysis. Part 2. Chemical and Microbiological Properties. American Society of Agronomy, Soil Science Society of America.
Pavlov, A.A., Kasting, J.F., 2002. Mass-independent fractionation of sulfur isotopes in Archean sediments: strong evidence for an anoxic Archean atmosphere. Astrobiology 2 (1), 27–41.
Pettijohn, F.J., 1975. Sedimentary rocks, third ed. Harper and Row, New York, pp. 628.
Pickard, A.L., 2003. SHRIMP U-Pb zircon ages for the Palaeoproterozoic Kuruman Iron Formation, northern Cape Province, South Africa: evidence for simultaneous BIF deposition on Kaapvaal and Pilbara cratons. Precambr. Res. 125 (3), 275–315.
Planavsky, N., Bekker, A., Rouxel, O.J., Kamber, B., Hofmann, A., Knudsen, A., Lyons, T.W., 2010. Rare earth element and yttrium compositions of Archean and Paleoproterozoic Fe formations revisited: new perspectives on the significance and mechanisms of deposition. Geochim. Cosmochim. Acta 74 (22), 6387–6405.
Planavsky, N.J., McGoldrick, P., Scott, C.T., Li, C., Reinhard, C.T., Kelly, A.E., Ellipsis & Lyons, T.W., 2011. Widespread iron-rich conditions in the mid-Proterozoic ocean. Nature 477 (7365), 448–451.
Planavsky, N.J., Asael, D., Hofman, A., Reinhard, C.T., Lalonde, S.V., Knudsen, A., Ellipsis & Beukes, N.J., 2014. Evidence for oxygenic photosynthesis half a billion years before the Great Oxidation Event. Nat. Geosci. 7 (4), 283–286.
Poitrasson, F., Halliday, A.N., Lee, D.C., Levasseur, S., Teutsch, N., 2004. Iron isotope differences between Earth, Moon, Mars and Vesta as possible records of contrasted accretion mechanisms. Earth Planet. Sci. Lett. 223 (3), 253–266.
Polyakov, V.B., Mineev, S.D., 2000. The use of Mössbauer spectroscopy in stable isotope geochemistry. Geochim. Cosmochim. Acta 64 (5), 849–865.
Poulton, S.W., Canfield, D.E., 2011. Ferruginous conditions: a dominant feature of the ocean through Earth's history. Elements 7 (2), 107–112.
Pourmand, A., Dauphas, N., Ireland, T.J., 2012. A novel extraction chromatography and MC-ICP-MS technique for rapid analysis of REE, Sc and Y: Revising CI-chondrite and Post-Archean Australian Shale (PAAS) abundances. Chem. Geol. 291, 38–54.
Quinn, K.A., Byrne, R.H., Schijf, J., 2004. Comparative scavenging of yttrium and the rare earth elements in seawater: competitive influences of solution and surface chemistry. Aquat. Geochem. 10 (1–2), 59–80.
Raiswell, R., 1982. Pyrite texture, isotopic composition and the availability of iron. Am. J. Sci. 282 (8), 1244–1263.
Rasmussen, B., Krapež, B., Meier, D.B., 2014. Replacement origin for hematite in 2.5 Ga banded iron formation: Evidence for postdepositional oxidation of iron-bearing minerals. Geol. Soc. Am. Bull. 126 (3–4), 438–446.
Rasmussen, B., Krapež, B., Muhling, J.R., Suvorova, A., 2015. Precipitation of iron silicate nanoparticles in early Precambrian oceans marks Earth's first iron age. Geology 43 (4), 303–306.
Rasmussen, B., Muhling, J.R., Suvorova, A., Krapež, B., 2016. Dust to dust: Evidence for the formation of "primary" hematite dust in banded iron formations via oxidation of iron silicate nanoparticles. Precambr. Res. 284, 49–63.
Rasmussen, B., Muhling, J.R., Suvorova, A., Krapež, B., 2017. Greenalite precipitation linked to the deposition of banded iron formations downslope from a late Archean carbonate platform. Precambr. Res. 290, 49–62.
Reinhard, C.T., Planavsky, N.J., Robbins, L.J., Partin, C.A., Gill, B.C., Lalonde, S.V., Ellipsis & Lyons, T.W., 2013. Proterozoic ocean redox and biogeochemical stasis. Proc. Natl. Acad. Sci. 110 (14), 5357–5362.
Riding, R., Fralick, P., Liang, L., 2014. Identification of an Archean marine oxygen oasis. Precambr. Res. 251, 232–237.
Rouxel, O., Dobbek, N., Ludden, J., Fouquet, Y., 2003. Iron isotope fractionation during oceanic crust alteration. Chem. Geol. 202 (1), 155–182.
Rouxel, O.J., Bekker, A., Edwards, K.J., 2005. Iron isotope constraints on the Archean and Paleoproterozoic ocean redox state. Science 307 (5712), 1088–1091.
Rouxel, O., Shanks, W.C., Bach, W., Edwards, K.J., 2008. Integrated Fe-and S-isotope study of seafloor hydrothermal vents at East Pacific Rise 9–10 N. Chem. Geol. 252 (3), 214–227.
Satkoski, A.M., Beukes, N.J., Li, W., Beard, B.L., Johnson, C.M., 2015. A redox-stratified ocean 3.2 billion years ago. Earth Planet. Sci. Lett. 430, 43–53.
Schauble, E.A., 2004. Applying stable isotope fractionation theory to new systems. Rev. Mineral. Geochem. 55 (1), 65–111.
Schieber, J., 1999. Microbial mats in terrigenous clastics; the challenge of identification in the rock record. Palaios 14 (1), 3–12.
Schoenberg, R., von Blanckenburg, F., 2005. An assessment of the accuracy of stable Fe isotope ratio measurements on samples with organic and inorganic matrices by high-resolution multicollector ICP-MS. Int. J. Mass Spectrom. 242 (2), 257–272.
Schoenberg, R., Marks, M.A., Schuessler, J.A., von Blanckenburg, F., Markl, G., 2009. Fe isotope systematics of coexisting amphibole and pyroxene in the alkaline igneous rock suite of the Ilímaussaq Complex, South Greenland. Chem. Geol. 258 (1), 65–77.
Schütte, S.S., 1992. Ongeluk Volcanism in Relation to the Kalahari Manganese Deposits (Doctoral dissertation).
Severmann, S., Johnson, C.M., Beard, B.L., German, C.R., Edmonds, H.N., Chiba, H., Green, D.R.H., 2004. The effect of plume processes on the Fe isotope composition of hydrothermally derived Fe in the deep ocean as inferred from the Rainbow vent site, Mid-Atlantic Ridge, 36 14′ N. Earth Planet. Sci. Lett. 225 (1), 63–76.
Sharma, M., Polizzotto, M., Anbar, A.D., 2001. Iron isotopes in hot springs along the Juan de Fuca Ridge. Earth Planet. Sci. Lett. 194 (1), 39–51.
Sholkovitz, E.R., Landing, W.M., Lewis, B.L., 1994. Ocean particle chemistry: the fractionation of rare earth elements between suspended particles and seawater. Geochim. Cosmochim. Acta 58 (6), 1567–1579.
Simonson, B.M., 1985. Sedimentological constraints on the origins of Precambrian iron-formations. Geol. Soc. Am. Bull. 96 (2), 244–252.
Skulan, J.L., Beard, B.L., Johnson, C.M., 2002. Kinetic and equilibrium Fe isotope fractionation between aqueous Fe (III) and hematite. Geochim. Cosmochim. Acta 66 (17), 2995–3015.
Smith, A.J., Beukes, N.J., Gutzmer, J., 2013. The composition and depositional environments of Mesoarchean iron formations of the West Rand group of the Witwatersrand Supergroup, South Africa. Econ. Geol. 108 (1), 111–134.
Summons, R.E., Bradley, A.S., Jahnke, L.L., Waldbauer, J.R., 2006. Steroids, triterpenoids and molecular oxygen. Philos. Trans. R. Soc. Lond. B Biol. Sci. 361 (1470), 951–968.
Sun, S., Konhauser, K.O., Kappler, A., Li, Y.L., 2015. Primary hematite in Neoarchean to Paleoproterozoic oceans. Geol. Soc. Am. Bull. 127 (5–6), 850–861.
Sun, S., Li, Y.L., 2017. Geneses and evolutions of iron-bearing minerals in banded iron formations of > 3760 to ca. 2200 million-year-old: Constraints from electron microscopic, X-ray diffraction and Mössbauer spectroscopic investigations. Precambr. Res. 289, 1–17.
Swart, Q.D., 2012. Carbonate rocks of the Paleoproterozoic Pretoria and Postmasburg

Groups, Transvaal Supergroup (Doctoral dissertation).
Teng, F.Z., Dauphas, N., Huang, S., Marty, B., 2013. Iron isotopic systematics of oceanic basalts. Geochim. Cosmochim. Acta 107, 12–26.
Tsikos, H., Beukes, N.J., Moore, J.M., Harris, C., 2003. Deposition, diagenesis, and secondary enrichment of metals in the Paleoproterozoic Hotazel iron formation, Kalahari manganese field, South Africa. Econ. Geol. 98 (7), 1449–1462.
Tsikos, H., Matthews, A., Erel, Y., Moore, J.M., 2010. Iron isotopes constrain biogeochemical redox cycling of iron and manganese in a Palaeoproterozoic stratified basin. Earth Planet. Sci. Lett. 298 (1), 125–134.
Waldbauer, J.R., Sherman, L.S., Sumner, D.Y., Summons, R.E., 2009. Late Archean molecular fossils from the Transvaal Supergroup record the antiquity of microbial diversity and aerobiosis. Precambr. Res. 169 (1), 28–47.
Welch, S.A., Beard, B.L., Johnson, C.M., Braterman, P.S., 2003. Kinetic and equilibrium Fe isotope fractionation between aqueous Fe (II) and Fe (III). Geochim. Cosmochim. Acta 67 (22), 4231–4250.
Widdel, F., Schnell, S., Heising, S., Ehrenreich, A., Assmus, B., Schink, B., 1993. Ferrous iron oxidation by anoxygenic phototrophic bacteria. Nature 362 (6423), 834–836.
Wiesli, R.A., Beard, B.L., Johnson, C.M., 2004. Experimental determination of Fe isotope fractionation between aqueous Fe (II), siderite and “green rust” in abiotic systems. Chem. Geol. 211 (3), 343–362.
Williams, L.A., Crerar, D.A., 1985. Silica diagenesis, II. general mechanisms. J. Sediment. Res. 55 (3).
Williams, H.M., McCammon, C.A., Peslier, A.H., Halliday, A.N., Teutsch, N., Levasseur, S., Burg, J.P., 2004. Iron isotope fractionation and the oxygen fugacity of the mantle. Science 304 (5677), 1656–1659.
Williams, H.M., Peslier, A.H., McCammon, C., Halliday, A.N., Levasseur, S., Teutsch, N., Burg, J.P., 2005. Systematic iron isotope variations in mantle rocks and minerals: the effects of partial melting and oxygen fugacity. Earth Planet. Sci. Lett. 235 (1), 435–452.
Zahnle, K., Claire, M., Catling, D., 2006. The loss of mass-independent fractionation in sulfur due to a Palaeoproterozoic collapse of atmospheric methane. Geobiology 4 (4), 271–283.
Zhang, J., Nozaki, Y., 1998. Behavior of rare earth elements in seawater at the ocean margin: a study along the slopes of the Sagami and Nankai troughs near Japan. Geochim. Cosmochim. Acta 62 (8), 1307–1317.